IDEA League

Master of Science in Applied Geophysics

Research Thesis

Local Crustal Imaging Using Distant High-Magnitude Earthquakes

Johno Egbart van IJsseldijk

August 10, 2018

Local Crustal Imaging Using Distant High-Magnitude Earthquakes

Master of Science Thesis

for the degree of Master of Science in Applied Geophysics at
Delft University of Technology
by

Johno Egbart van IJsseldijk

August 10, 2018

Department of Geoscience & Engineering · Delft University of Technology

Delft University of Technology

Printed in The Netherlands

IDEA LEAGUE
JOINT MASTER'S IN APPLIED GEOPHYSICS

Delft University of Technology, The Netherlands
ETH Zürich, Switzerland
RWTH Aachen, Germany

Dated: *August 10, 2018*

Committee Members:

Dr. Cornelis Weemstra[1]

Prof. Florian Wellmann[2]

Dr. Elmer Ruigrok[3]

Drs. Arie Verdel[4]

Supervisor(s):

Dr. Cornelis Weemstra[1]

Dr. Elmer Ruigrok[3]

Drs. Arie Verdel[4]

[1]Delft, University of Technology & KNMI
[2]RWTH Aachen University
[3]KNMI & Utrecht University
[4]TNO, Utrecht

Abstract

Global phases are seismic waves that travel through the earth's core before emerging at the surface. Traditionally, global phases are used to obtain subsurface information up to 1 Hz. A recent study, however, found that signal present in the coda of strong, distant earthquakes contains higher frequencies. Quantitative analysis of the coda of earthquakes, of at least magnitude 6, shows that frequencies of, on average, 3 Hz can be found, with the most promising results coming from P- and PKIKP-phases. By autocorrelating the coda of these phases an estimate of the zero-offset reflection response below a seismic station can be retrieved.
The method allows to successfully delineate basins in both Argentina and the United States. Even higher frequencies, up to 8 Hz, are used at specific stations, that have been active for an extended period of time ($\geq$ 8 years). Again the method succeeds in retrieving structural information below these stations. The results of both studies are confirmed by existing literature as well as Ambient Noise Seismic Interferometry (ANSI) studies. ANSI is a method, which retrieves the reflection response below a station by applying seismic interferometry to ambient noise.
Advantages are that the method is computationally cheap and fast and that it is a passive measurement thus requiring low-effort. A disadvantage, however, is the unpredictability of earthquakes, which means that the exact duration the stations have to be active is unknown. Instead, the station will have to record over a prolonged amount of time, during which suitable earthquakes should occur. Research into the upper crustal structure, in particular, may benefit from the method. For example, the depth of a sedimentary basin can be discovered and imaged using this method. This gives important constraints, e.g. for geothermal prospecting.

Acknowledgements

First of all, I would like to thank my three supervisors: Kees Weemstra, Elmer Ruigrok, and Arie Verdel. I feel privileged to have been able to work with such intelligent people and I utterly enjoyed our time working together.
My day-to-day supervisor, Arie, was the first person I would run to, both with problems as well as with promising results. I want to thank him for always being available for having lengthy and, more importantly, fruitful discussions. His everlasting enthusiasm helped me continue even at the times when the data seemed to be not on my side.
For technical support, I could always turn to Elmer, who assisted me with the Matlab implementation of the different packages and scripts. I would also like to thank him for sharing some of his amazing Matlab codes, which enabled me to speed up my research. Not only did he prove to be very helpful for the computational side of my research, he also helped me in learning the fundamentals of earthquake seismology.
Last but not least I would like to thank Kees, who always provided thoughtful and diligent feedback in our meetings. His constructive comments in these meetings pushed me to work accurately and to back up my findings with sufficient amounts of evidence. Consequently, the quality of this thesis was ensured by his thorough input.
Finally, I am grateful to all three of my supervisors for their careful review and insightful comments on the thesis, which drastically improved this final version.
I want to thank TNO for giving me the opportunity to work in a professional environment and allowing me to use their resources. I thank my colleagues at TNO for the weekly squash sessions. Furthermore, special thanks to the fellow interns in the office, who made my time at TNO both a pleasant as well as an educational experience. I enjoyed the many coffee breaks and lunches together, which were always a welcome interruption during a hard day's work. In particular, I would like to thank Henry Brett for the friendly banter and the many discussions about ANSI and the project.
Moreover, I would like to thank my family and friends for enduring me rambling on about the project, my sister for cooking my dinner once, as well as Billie for putting up with me being away from home for so long during my studies and this thesis project.

A great number of online resources and toolboxes were used for this research, I am extremely

grateful for all the people that contributed to these tools and helped in making these resources freely available for use.
For the Malargüe array data, I thank Incorporated Research Institutions for Seismology-Program for Array Seismic Studies of the Continental Lithosphere (IRIS-PASSCAL) for providing the seismic equipment and the Argentine Ministry of Science, Technology, and Production Innovation for the financial support connected to the transport of the equipment. I also thank Pierre Auger and the Department of Civil Defense of Malargüe for the help during the data acquisition.
Furthermore, I thank the contributors to the SPREE-project. This project was funded by the National Science Foundation through EarthScope and was enabled by dozens of landowners and park rangers that allowed and assisted with installing and running the stations on their land.
The facilities of IRIS Data Services, and specifically the IRIS Data Management Center were used for access to waveforms, related metadata, and/or derived products used in this study. Data from the TA network were made freely available as part of the EarthScope USArray facility, operated by the IRIS. IRIS Data Services are funded through the Seismological Facilities for the Advancement of Geoscience and EarthScope (SAGE) Proposal of the National Science Foundation under Cooperative Agreement EAR-1261681.
Moreover, I would like to thank OpenStreetMap (https://www.openstreetmap.org/) and their contributors as well as Stamen Design (http://maps.stamen.com/) making their maps freely available for use. As well as QGis (https://qgis.org/) and their contributors for making their software freely available. I also want to thank the contributors to the M_Map package in Matlab (https://www.eoas.ubc.ca/~rich/map.html), which was used to make some of the maps in this thesis.
I thank MatTauP (https://github.com/g2e/seizmo/tree/master/mattaup), which was used to calculate ray paths, ray parameters and arrival times. Finally, I thank the contributors and sponsors of the CREWES Matlab Library (https://www.crewes.org/), which was used to calculate Fourier transforms and display traces.

Delft University of Technology
August 10, 2018

Johno Egbart van IJsseldijk

Table of Contents

List of Figures

Acronyms

AC	Autocorrelation
ANSI	Ambient Noise Seismic Interferometry
ETH	Swiss Federal Institute of Technology
FD SNR	Frequency Domain SNR
GLIMPCE	Great Lakes International Multidisciplinary Program on Crustal Evolution
GloPHV	Global Phase H/V Spectral Ratio
GloPSI	Global Phase Seismic Interferometry
GloPSI HF	High Frequency GloPSI
IRIS	Incorporated Research Institutions for Seismology
KNMI	Royal Netherlands Meteorological Institute
LVZ	Low Velocity Zone
RWTH	Aachen University
SI	Seismic Interferometry
SNR	Signal to Noise Ratio
SPREE	Superior Province Rifting Earthscope Experiment
TD SNR	Time Domain SNR
TNO	Netherlands Organisation for Applied Scientific Research
TUD	Delft University of Technology
TWT	Two-way Time

Chapter 1

Introduction

A recent study by Verdel et al. (2016) in Reykjanes, Iceland, has shown that high frequency signal (3-8 Hz) can be observed in the coda of strong, distant earthquakes. The signal can then be autocorrelated to create zero-offset reflection responses. From these responses, structural information of the local crust is obtained.
In the past, global phases phases have been used to retrieve compressional wave reflectivity images (e.g. Ruigrok and Wapenaar (2012) and Nishitsuji et al. (2016)). Global phases are seismic waves that travel through the core before reaching the surface. By autocorrelation of global phases the zero-offset P-wave reflectivity below a station is extracted. This method, known as Global Phase Seismic Interferometry (GloPSI), benefits from the advantages of global phases. First, the small angles of incidence, imply large source Fresnel zones. Consequently, the area over which the global phases are induced is large, making the method viable even for areas sparsely populated with seismicity. Secondly, the vertical-component of global phases already approximates the P-wave transmission response well, allowing to disregard the horizontal components with a lower signal-to-noise ratio (Ruigrok and Wapenaar, 2012). However, these GloPSI studies limit themselves to frequencies below 1 Hz. GloPSI HF (high frequency GloPSI, the method proposed in this study) should in principle obtain near-surface reflectivity of higher resolution, by including higher frequencies present in the coda of very strong events. A fraction of the teleseismic phases, viz. phases solely traveling through the mantle, also possess small angles of incidence, provided they originate from large distances. These teleseismic phases are also tested in this study. This research, therefore, aims to use high frequency data ($>$ 1 Hz) from large magnitude earthquakes to estimate local zero-offset reflection responses, providing near-surface structural and velocity-depth information of the crust.
This is accomplished in two stages. First, a quantitative approach is used to determine which events are suitable, with respect to magnitude, distance and ray parameter, for autocorrelation. After the optimal parameters have been established and the viability of the method has been tested, a second, qualitative approach aims to apply the technique on array data and compare/evaluate the results with earlier studies in the area of interest.
In the first stage, a selection of stations of the US Transportable Array is made. This selection consists of broadband stations with an extensive lifespan ($\geq$7 years) to ensure

that the data includes multiple very high magnitude earthquakes (≥8 Mw). Next, the ray-parameter, maximum frequency, and corner frequency are determined for each station-event combination. For this analysis, not only different events and stations are considered, but also a separation between different seismic phases is made.
The results of the quantitative analysis will then allow for making a selection of suitable events for the second part, where the proposed technique is tested on data from the SPREE-array in the US (Van Der Lee et al., 2013) as well as the Malargüe-array in Argentina (Ruigrok et al., 2012) and (Weemstra et al., 2017). Both spectral whitening and band-pass filtering will be applied prior to autocorrelation, after which the data for each station will be stacked resulting in a 2D section. These sections will be compared to results of earlier studies to assess the accuracy of the method. Finally, an ambient noise seismic interferometry (ANSI) study will be conducted for comparison. This method retrieves the seismic reflection response below a station by applying seismic interferometry to ambient noise, and has been applied successfully in the past for shallow (upto $\sim$ 3 km deep) (e.g. Boullenger et al. (2014); Verdel et al. (2016)) and deep crustal research (e.g. Tibuleac and von Seggern (2012); Oren and Nowack (2016)). However, ANSI studies on the upper crustal structure (4 to 10 km deep) are still relatively limited. A recent study by Romero and Schimmel (2018) managed to map a sedimentary basin using ANSI, but the spacing between stations in this study is still quite coarse (ranging from 10 km to 150 km). Therefore, this study also aims to retrieve structural information below an array of stations (with denser spacing) using ANSI.
Unfortunately, due to the limited amount of the data for both the SPREE-array ($\sim$ 2 years) and Malargüe-array ($\sim$ 1 year), insufficient events with sufficiently high frequencies could be selected. Consequently, the final frequency band for the sections was between 1.25 and 3 Hz. In order to also consider the very high-frequency band (3 - 8 Hz) the US Transportable Array will be considered once more. Two ideal stations with multiple high frequency events are selected from the data. GloPSI HF is then applied to find the reflectivity below these stations. Lastly, the results are compared with an ANSI study performed on the same stations.

Part I

Theory and quantitative analysis of the spectra of the coda

Chapter 2

Theory

This chapter will first provide a brief description of seismic phases followed by an explanation of seismic interferometry.

2-1 Seismic phases

This section briefly recaps seismic phases, which indicate how a ray travels through the earth. Since waves can behave differently throughout the layers in the earth, one source will cause a variety of different phases. Not all phases will be suitable for autocorrelation because a small angle of incidence is required to retrieve a meaningful zero-offset measurement, as will be discussed in detail in the next section. The phases, that are considered in this research are listed below. Please note that only compressional waves are considered.

- P: Wave that travels solely through the mantle.
- PP: Wave propagating through the mantle only, with one reflection at the surface.
- Pdiff: The wave gets diffracted at the core-mantle boundary.
- PcP: This wave is reflected at the core-mantle boundary.
- PKP: This wave travels through the outer core.
- PKiKP: Wave propagating through the mantle and outer core, reflected at the inner core.
- PKIKP: Wave traveling through the mantle and both the inner and outer core.

Figure 2-1 shows an example of the path for each phase. Please note that this list is far from complete, however. Other phases (e.g. shear waves or multiple reflections) are not relevant for this study. For those interested, Storchak et al. (2003) provide an excellent overview of the nomenclature of seismic phases.

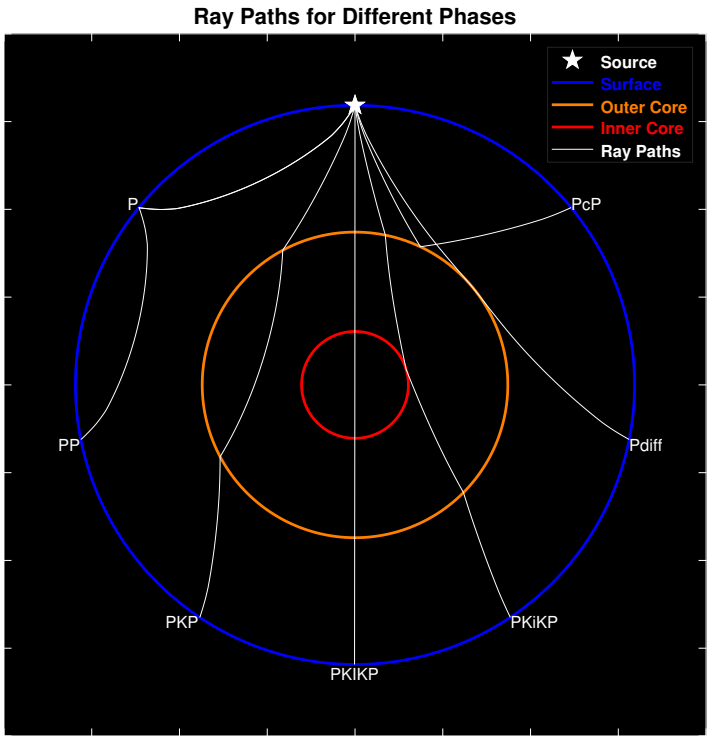

Figure 2-1: Example of ray paths (white) for different phases, modelled with the IASP91 spherical model (Kennett and Engdahl, 1991) using the TauP toolkit (Crotwell et al., 1999). The three circles represent the outer boundary of the solid earth (blue), the outer core (orange) and the inner core (red). The rays originate from the same source (white star), but different paths have different phase names.

2-2 Seismic interferometry

Seismic interferometry is a technique that allows for virtual sources to be placed at the location of a receiver, the response to this virtual source is then recorded at another receiver by means of simple crosscorrelations. It allows retrieval of the Green's function of the earth between two stations (a virtual source and a receiver), without knowing the origin of the real source(s) (Wapenaar et al., 2010). In this thesis, seismic interferometry will be both applied to the coda of distant earthquakes as well as to ambient noise, known as ambient noise seismic interferometry (ANSI). This section gives a brief overview of seismic interferometry; for a more detailed discussion, the tutorial paper by Wapenaar et al. (2010) is recommended.

Global Phase Seismic Interferometry

Claerbout (1968) first found that one can retrieve the 1D reflection response of a layered medium by autocorrelation of an incident plane-wave coming from the lower half-space. In other words, by autocorrelation of the transmission response one can obtain the reflection response (Wapenaar et al., 2010):

$$R(t) + R(-t) - \delta(t) = -T(t) * T(-t) \tag{2-1}$$

Here $R(+t)$ and $R(-t)$ denote the causal and anti-causal reflection response, respectively, $\delta(t)$ the illuminating wavefield and T the transmission response (Wapenaar et al., 2010). The autocorrelation is found on the right-hand side of the equation since the convolution (denoted with $*$) of a function with its time-reversed version is equal to the autocorrelation of that function. In our case, the transmission response coincides with the direct wave and coda of the selected earthquake phase. The coda, derived from the Latin word for tail, are the back-scattered waves due to an incoming phase.
For a better understanding of why autocorrelation of the transmission response reveals reflection information, it is important to realize that the reflection response with its multiples is included in the transmission response as well. After all, the incoming wave (transmitted through a layer x) is reflected at the free surface (with, in 1D, a reflection coefficient of -1) and then reflected back towards the surface again by the same layer x with a coefficient of r. This results in an alternating pattern recorded by the receiver (assuming a loss-less medium) of $\tau, -\tau r, \tau r^2, -\tau r^3$... and so on. Where τ is the transmission through the layer x (first arrival), all other terms are multiples due to the reflections at the bottom of layer x (Wapenaar et al., 2010).
Equation 2-1 is only valid for perfectly horizontally layered media and a delta pulse source function. However, in reality the source function is not a single pulse, but rather a source time function, which will distort the transmission response. Moreover, illumination from multiple angles is required to image slightly dipping layers (as opposed to a perfectly horizontal medium). Consequently, Equation 2-1 is adapted to (Ruigrok and Wapenaar, 2012):

$$\{R(t) + R(-t) - \delta(t)\} * S_n(t) \propto -\sum_{\theta_{\min}}^{\theta_{\max}} \sum_{p_{\min}}^{p_{\max}} T(\mathbf{p}, -t) * s_i(-t) * T(\mathbf{p}, t) * s_i(t) \tag{2-2}$$

Here $\mathbf{p} = (p, \theta)$, with p the absolute horizontal ray parameter and θ the back azimuth. $s_i(t)$ is the source time function of the i-th source and $S_n(t)$ is the average of autocorrelations of the different source time functions (Ruigrok and Wapenaar, 2012). By stacking multiple global phases the desired illumination from different angles is achieved, thus improving the wavenumber (or ray parameter) resolution. Moreover, the stacking also suppresses source side effects, while enhancing the stationary events (Snieder, 2004; Ruigrok et al., 2010).
As stated, the theory is based on an incoming plane-wave from below the layered medium. Whereas, earthquakes behave like point sources generating spherical-waves. However, at large distances a spherical-wave can be approximated as a plane-wave, therefore only earthquakes at large distances are considered. Secondly, the waves have to originate from below the medium of interest, and the wave is required to have a sufficiently small angle of incidence with the receiver. This ensures that the information is coming from directly below the station, therefore making the reflection response approximating a zero-offset measurement. For this

reason, only the phases in Figure 2-1 are considered, as these phases all have a small angle of incidence (for P- and PP-phases this is only true at large distances).
For the implementation of GloPSI to high frequencies, from now on referred to as GloPSI HF, Equation 2-2 does not change. However, for P-phases the ray parameter varies from $p_{\min} \approx 0.04$ s/km to $p_{\max} \approx 0.045$ s/km, as opposed to $p_{\min} = 0$ s/km to $p_{\max} \approx 0.04$ s/km for global phases (Ruigrok and Wapenaar, 2012). This means that solely using P-phases will result in an illumination gap for low ray parameters (≤ 0.04 s/km). However, global phases can be used in conjunction with P-phases, in order to provide complementary illumination in the low ray parameter range.

Noise interferometry

Equation 2-1 can be extended for ambient noise seismic interferometry (ANSI) (Wapenaar et al., 2010):

$$\{R(t) + R(-t)\} * S_n(t) - S_n(t) = -\langle u(t) * u(-t) \rangle \tag{2-3}$$

Where $S_n(t)$ is the autocorrelation of the noise and $u(t) = T(t) * N(t)$ is the transmission response convolved with the noise signal. $\langle \cdot \rangle$ denotes ensemble averaging, which, in practice, is replaced by an integration over sufficiently long time. Once again knowing the position of the real source(s) is not required (Wapenaar et al., 2010).
To obtain the reflection response from Equation 2-3 the autocorrelation of the source time function of the noise sources ($S_n(t)$) has to be removed. This is done by assuming this autocorrelation to be constant within the used frequency range of 3 to 8 Hz (Verdel et al., 2016). With this limitation information can still be obtained up to a few km depth as previous studies have shown (Draganov et al., 2007, 2009; Verdel et al., 2016).
Moreover, $u(t)$ is the recorded response at the receiver. To achieve a sufficiently high SNR, multiple autocorrelations are stacked over a long period of time (denoted in the formula by the ensemble averaging). This is the main difference between ANSI and GloPSI: for ANSI multiple (> 100) autocorrelations have to be stacked together, for GloPSI, on the other hand, only a few (~ 10) autocorrelations are needed to retrieve a reflection response. This also implies that GloPSI is computationally a lot less expensive compared to ANSI.
Another important difference between the two equations is, that Equation 2-1 is applicable for incoming plane waves, whereas Equation 2-3 is applicable for transient and noise signals. Consequently, the virtual sources for GloPSI are impulsive plane waves, while the virtual sources for ANSI are transient point sources (Wapenaar et al., 2010). Because of this difference, a geometrical spreading-correction is required for the reflection response retrieved with ANSI, but not for the reflection response of GloPSI.

Chapter 3

Methods

This chapter discusses the data acquisition and processing. This includes retrieving waveforms and earthquake events from the Incorporated Research Institutions for Seismology (IRIS) database. Thereafter some processing will be done on the data to retrieve important parameters and information regarding e.g. the distance, ray parameter and maximum frequency with high SNR. This data, for each station-event combination, will be separately stored in a "meta-data" database, which can be used to better analyze the retrieved data. Figure 3-1 shows these processes schematically.

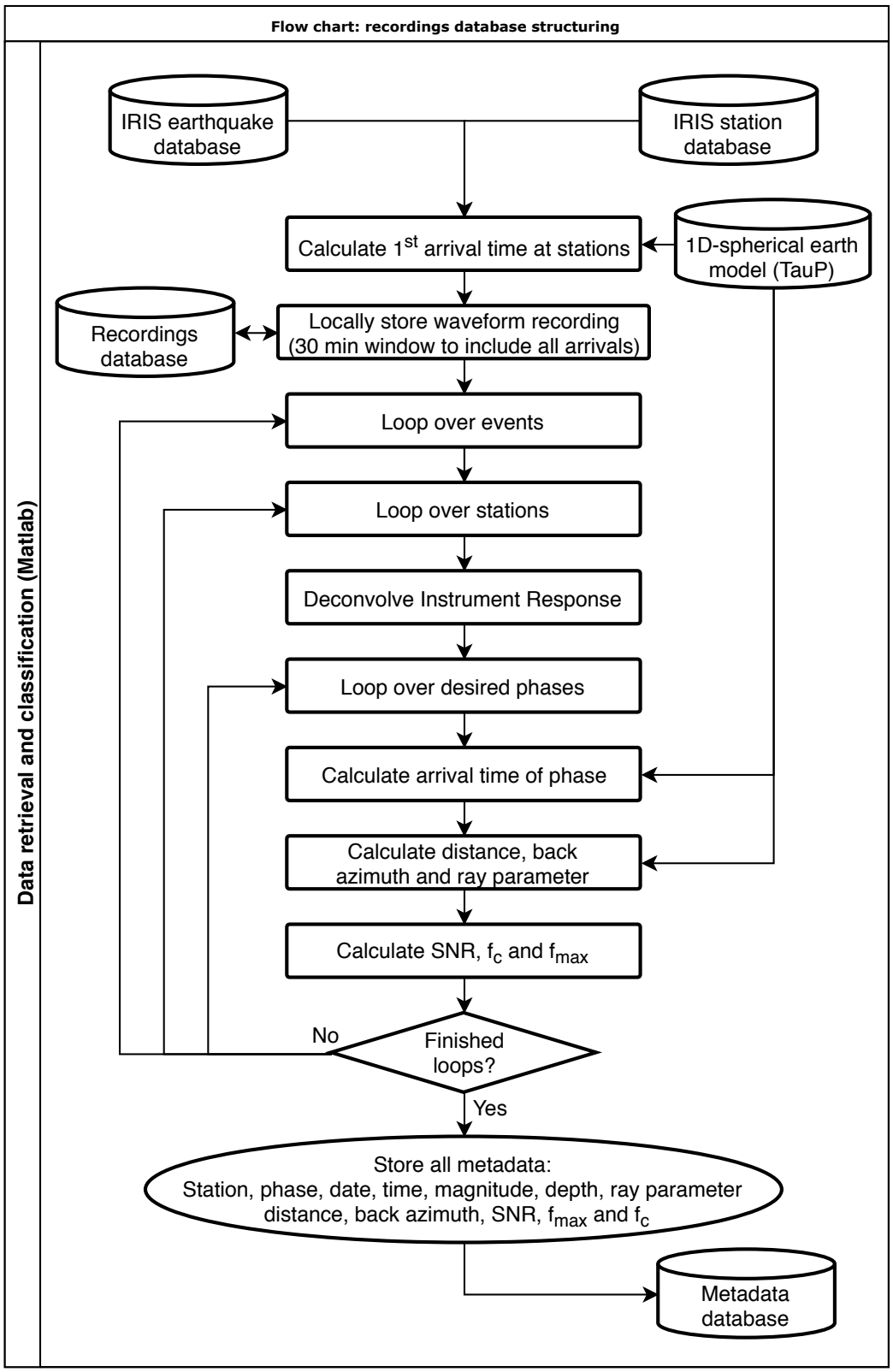

Figure 3-1: Flowchart showing the acquisition and first processing of the data for later analysis.

3-1 Data acquisition

All data, earthquake parameters as well as station parameters, are retrieved from the IRIS database. From the earthquake catalog, only events with a magnitude greater than 6.0 are selected. This is done partly due to time and memory constraints, but also because low magnitude events most likely result in global phase arrivals that do not possess sufficient energy for our purposes. For the first part, a selection of stations from the US transportable array is made, this is needed because with 1414 stations in total the data set would simply be too large and therefore time-consuming for our analysis. To reduce the number of stations, only stations that existed before 2011 and still active at present are considered. Moreover, by limiting the selection to the central part of the US, the total number of stations used for the analysis is brought down to 21 stations, shown in Figure 3-2. The long lifetime of these stations ensures that a decent number of (very) high magnitude earthquakes are recorded: in total 11 earthquakes with a magnitude greater than 8, almost 200 earthquakes greater than 7, and about 1800 earthquakes greater than 6.
For each earthquake, the expected first arrival and ray parameter are calculated using the TauP toolkit (Crotwell et al., 1999). The station's recording is then retrieved from the IRIS database, starting 5 minutes before the expected arrival and ending 25 minutes after. The data is then deconvolved with the instrument response of the station; this converts the raw signal from digital counts to m/s. This deconvolution is only applied once for each trace, after which the time-window for each phase is selected from the deconvolved data.

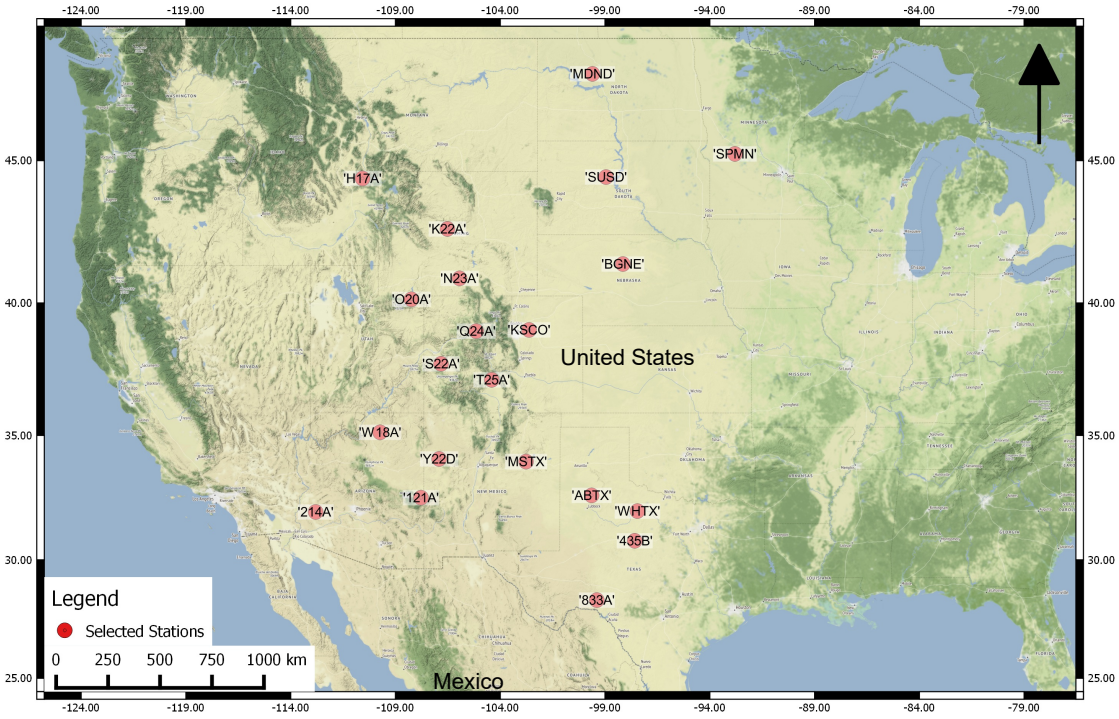

Figure 3-2: The 21 selected stations of the transportable USArray (red). Map tiles by Stamen Design (2011), under CC BY 3.0. Data by OpenStreetMap contributors (2004), under ODbL.

3-2 Signal to noise ratio and maximum frequency

An important parameter for the autocorrelations is the maximum frequency ($f_{\max}$) at which there is still (sufficient) signal in the coda. Two different signal to noise ratios (SNR) are considered in this thesis, on in the time domain (TD SNR) and one in the frequency domain (FD SNR). The TD SNR is determined, by setting the signal to the first 2 minutes after the arrival of a phase and the noise is set to the 2 minutes at the start of the recording (5 minutes before the arrival of the first phase). This is done on unfiltered data, with only the instrument response removed.
The FD SNR is then fitted with a Gaussian ($a \exp\left(-\frac{(x-b)^2}{2\ c^2}\right)$), using a least-squares fit. Finally, the frequency at which the FD SNR fit is greater than 5 dB is selected as $f_{\max}$. An example of this approach is shown in Figure 3-3.
The SNR (both FD and TD) is also important for determining how strong the signal for each phase is, which yields useful insights into which phases are more likely to provide successful results. The next section will discuss the ray parameter, another important criterion for determining suitable phases.

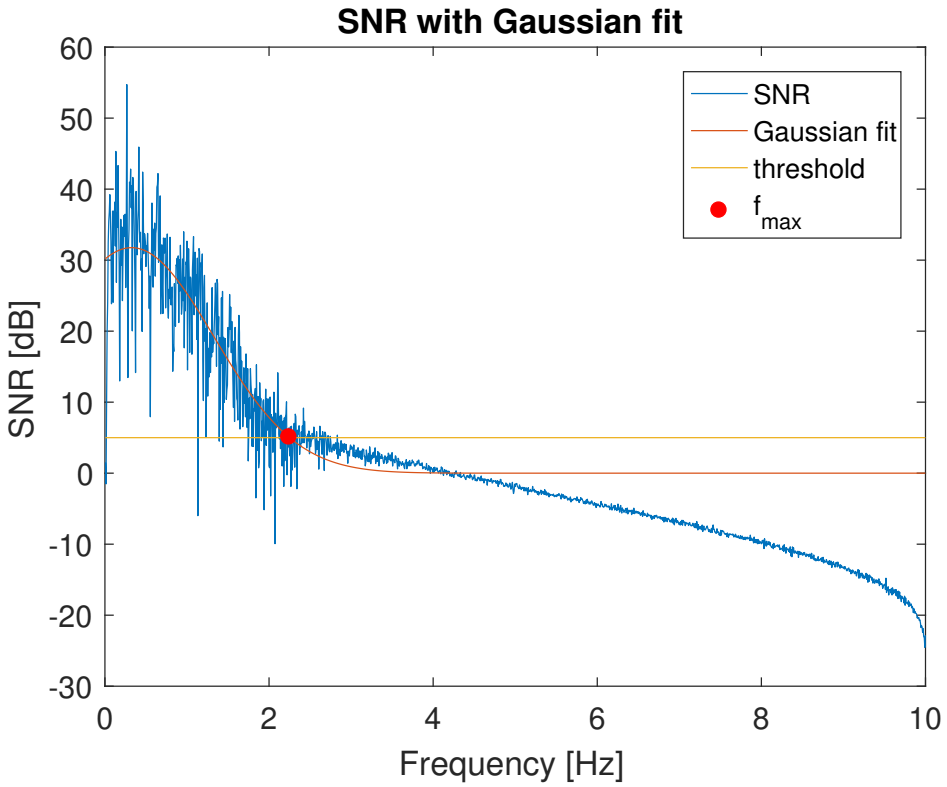

Figure 3-3: FD SNR in dB (blue) with it's fit (red) as a function of frequency. The largest frequency at which the SNR-fit is larger than the threshold of 5 dB (yellow) is defined as $f_{\max}$ (red dot).

3-3 Ray parameter

In the previous section, the SNR was discussed as a parameter to evaluate the quality of different phases. The ray parameter is another important criterion for the selection of the phases. The ray parameter (p) is the horizontal slowness of the incident wavefront (assuming the earth as a radially symmetric sphere) (Shearer, 2009). Recall that the incident waves should be nearly vertical to ensure that the resulting autocorrelations can be interpreted as zero-offset reflection responses. This implies that the ray parameter should be as small as possible to achieve the best results. Figure 3-4 shows the ray parameter as a function of distance for different phases, please note that the ray parameters are computed using the TauP toolkit (Crotwell et al., 1999), and they are not estimated based on the waveform data. From this figure, it can be concluded that the PKiKP- and PKIKP-phases have the lowest, and therefore, optimal ray parameters, viz. these phases arrive almost vertically at the earth's surfaces. Secondly the PKP- and Pdiff-phases, as well as P-phase at large ($\geq$70 degrees) distances, also display a relatively low ray parameter. It should also be noted that, even though PcP-waves have a low ray parameter, they are generally not suitable for autocorrelation, because they are overwhelmed by the arrival of direct S-waves and surface waves.

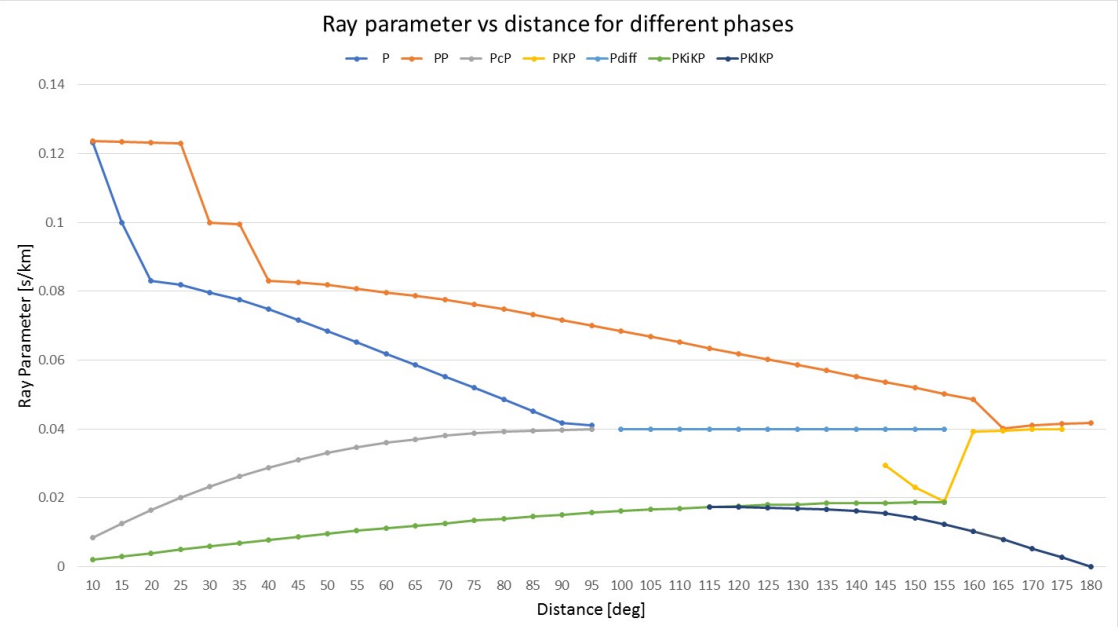

Figure 3-4: The Ray Parameter as a function of distance, different colors indicate different phases. The graph was created using modelled data, using the TauP toolkit (Crotwell et al., 1999) ant the IASP91 earth model (Kennett and Engdahl, 1991) with an event depth of 0 km.

3-4 Spectral fit and corner frequency

The final parameter that will be discussed is the corner frequency, which indicates the frequency at which the amplitude decay begins, as shown in Figure 3-5. Although, this parameter is not required for seismic interferometry, it does help to assess which phases are most suitable for GloPSI HF. It is also interesting to assess how the corner frequencies of the events compare to the expected values based on theoretical models. Furthermore, it also illustrates what the spectra of the earthquake coda approximately look like.
Figure 3-5 shows the modeled amplitude spectra for different magnitude earthquakes, and is based on the Madariaga model (Madariaga, 1976). This source-side model predicts the P-wave spectra from results of dynamic calculations for a circular fault using finite differences, assuming a rupture velocity of 90% of the shear-wave velocity. The spectra can be described by two effects: first, there is the long-period spectral level (Ω_0), which indicates the amplitude before any decay, secondly there is the corner frequency, where the decay starts (Shearer, 2009). These two effects compete with each other: higher magnitude earthquakes have a higher Ω_0, but their corner frequency is lower so the amplitude decay starts at lower frequencies. If the first "Ω_0-effect" dominates, greater magnitudes would also produce greater amplitudes at high frequencies. However, if the second "corner frequency-effect" is stronger, the contrary would be true. It is therefore interesting to evaluate how this theoretical spectral behavior is observed in reality, and especially this trade-off between Ω_0 and f_c, as this could mean that lower magnitude events could still provide meaningful insights.
As stated, Figure 3-5 looks at the source side of the problem, however, in our case the receiver side will be recorded. To correct for this, viz. to include wave propagation as well as (source and receiver) site-specific effects, Dost et al. (2018) add two more terms to approximate the spectrum at the receiver side:

$$A(f) = \Omega_0 \frac{S(f)}{(1 + (f/f_c)^4)^{1/2}} e^{-\pi f t^*} \tag{3-1}$$

In Equation 3-1 Ω_0 and f_c are the long-period spectral level and the corner frequency, respectively. The additional parameter $S(f)$ is included for receiver site-specific effects and the exponential term with t^* is a correction for propagation and attenuation in the earth (Dost et al., 2018).
The data can now be fitted according to the formula using a least-squares approximation, using the trust-region-reflective algorithm (Moré and Sorensen, 1983). Although Equation 3-1 has 4 constants (Ω_0, f_c, $S(f)$ and t^*), for the least-squares fit Ω_0 and $S(f)$ are combined to one constant, due to the ambiguity in fitting a product. Usually $S(f)$ is assumed to be 1 to solve this problem (Dost et al., 2018). An example of the fitting function is shown in Figure 3-6.
To recreate Figure 3-5 Ω_0 is set to moment magnitude M_0, which can be approximated from the magnitude of the event (Shearer, 2009):

$$M_0 = 10^{\frac{3}{2}M_W + 9.1} \tag{3-2}$$

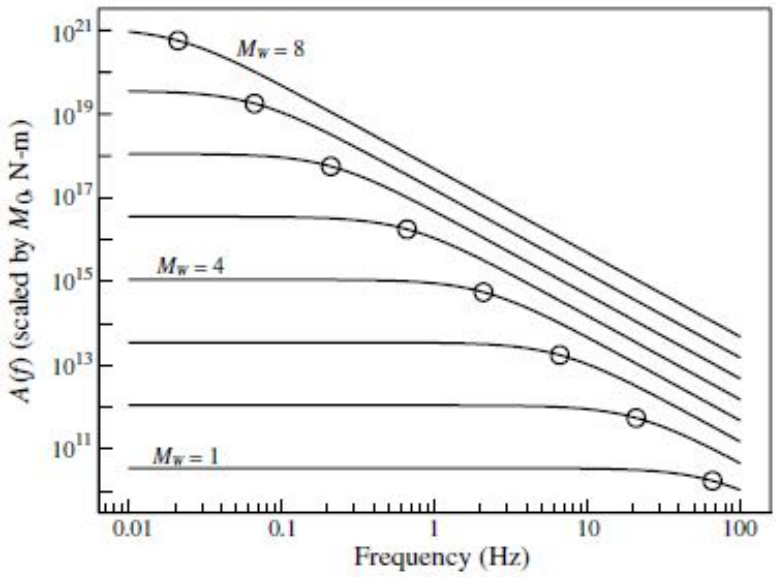

Figure 3-5: Predicted P-wave spectrum for different-magnitude earthquakes using the Madariaga (1976) source model. Corner frequencies f_c are indicated by circles. (Shearer, 2009).

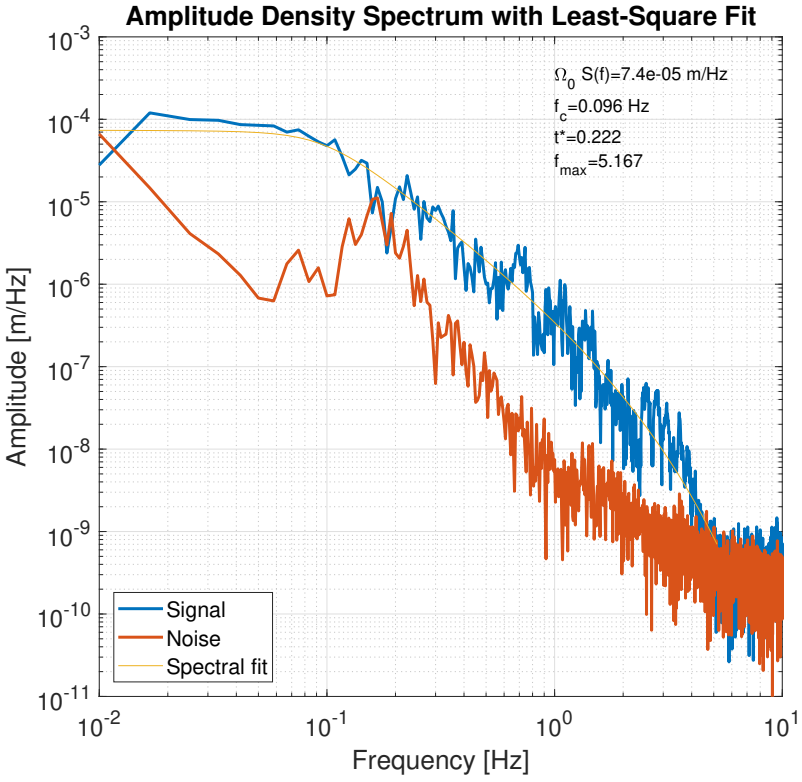

Figure 3-6: An example of the fitting function, shown are the signal (blue), it's fit (yellow), and also the noise recording (red) for reference. The value of the fitting parameters (Equation 3-1) are shown in the top right, f_{max} is derived using a Gaussian fit, similar to Figure 3-3. The "bump" in the noise at 0.1 Hz is caused by the microseisms.

Chapter 4

Results part 1

The following section will discuss the results of the previously described method on the data for the selection of the US Array stations. Again, only earthquakes with a magnitude greater than 6 are considered. First, the signal to noise ratio for each phase will be discussed. Then the value of $f_{\max}$ versus distance and magnitude is calculated. Finally, the corner frequency is fitted and the expected amplitude spectra for different magnitudes are reviewed.

4-1 TD SNR for different phases

For the TD SNR analysis, only the following phases are considered: P, Pdiff, PKP, PKiKP, PKIKP, and PP. All of these phases have a sufficiently low ray parameter (less than 0.05 s/km, corresponding to an angle of incidence of 16.9 degrees with the vertical using the average top crustal layer velocity of 5.8 km/s of the IASP91 model (Kennett and Engdahl, 1991)), although sometimes only at certain distances (as shown in Figure 3-4).
In Figure 4-1 the TD SNR is plotted against distance for each phase. The TD SNR was determined by comparing 120 seconds of signal to recorded noise of the same length. Because phases sometimes arrive at the similar times there can be some ambiguity as to which arrival is recorded. To also include these effects the overlap with other phases is displayed at the bottom of the plots. The maximum amount of overlap is equal to 120s, which would mean the phases arrived at exactly the same time. The overlap then decreases for arrivals before or after the desired phase's arrival.
It should be noted that for small distances (*leq* 30 degrees) the P- and PP-phases do not yet exist, instead so called crustal phases are observed at these distances (Storchak et al., 2003). Moreover, the peak in TD SNR for PKiKP waves at small distances (*leq* 40 degrees) is due to the overlap with S-phases in this range. However, since only large distances are of interest for this study, these small distance effects can be ignored. From the figure, it is apparent that at large distances, of 140 degrees and higher, there is a lot of overlap between the PKiKP, PKIKP and PKP phases. Furthermore, there is some overlap of PP- and PKiKP-waves in the 90 - 120-degree range. It can also be noted that the TD SNR is generally decreasing with

increasing distance. Moreover, the TD SNR seems to be relatively high (≥5 dB) for most phases, except for the Pdiff-arrivals (4-1(b)). Furthermore, it should also be noted that at around 140-150 degrees there is a peak in the TD SNR for the PKP and PKiKP phase, which is due to PKP-triplications.

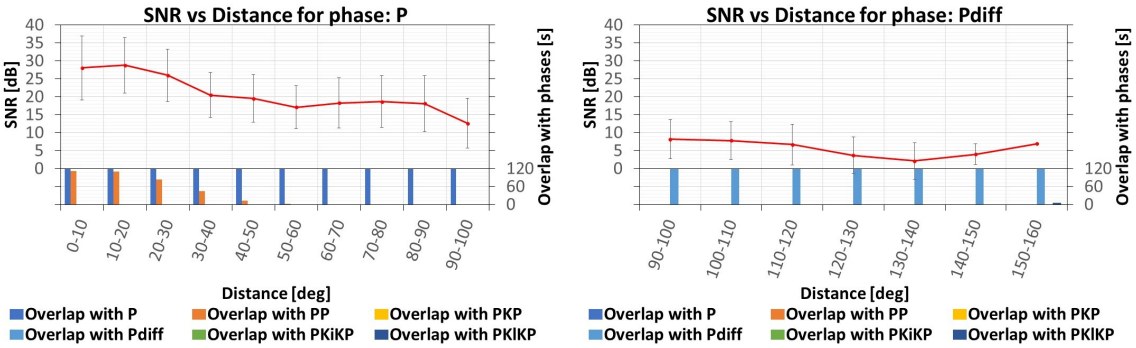

(a) TD SNR for P-waves

(b) TD SNR for Pdiff-waves.

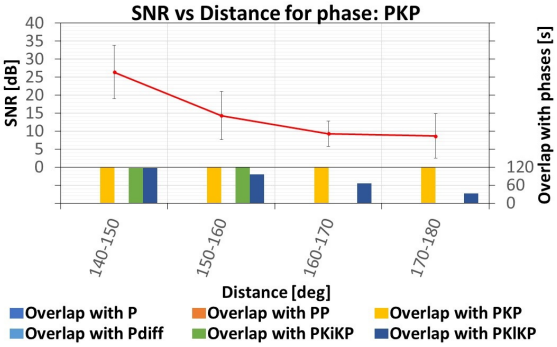

(c) TD SNR for PKP-waves

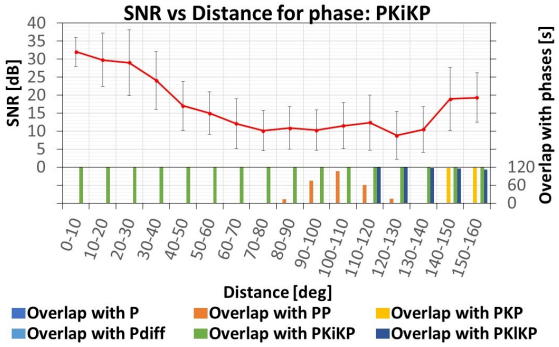

(d) TD SNR for PKiKP-waves.

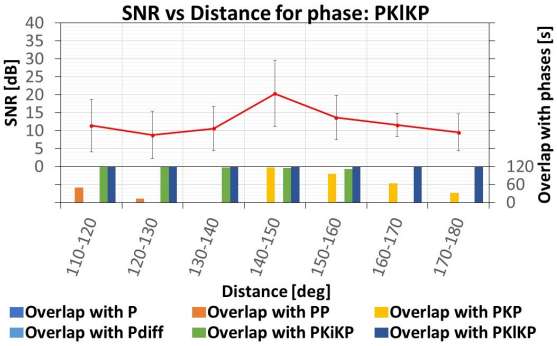

(e) TD SNR for PKIKP-waves

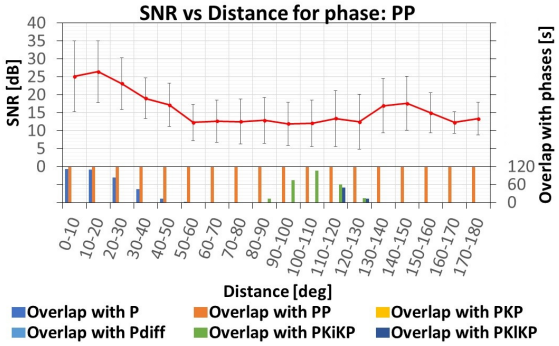

(f) TD SNR for PP-waves.

Figure 4-1: TD SNR graphs (red) for different phases, one side of the error bar represents 1 standard deviation. The bars at the bottom of each graph represent the amount of overlap with other phases in the selected time window of 120 seconds, therefore each phase has 120s (100%) overlap with itself.

4-2 Maximum frequency

One of the most important parameters for our analysis is the maximum "usable" frequency, as previously stated this is the frequency at which the FD SNR is still greater than 5 dB. Figure 4-2 shows plots the average of $f_{\max}$ against distance (4-2(a)), and against magnitude (4-2(b)). All phases have been included for this analysis, instead of considering each phase individually as was previously the case. We clearly observe how $f_{\max}$ decreases with increasing distance, the slight peak around 145-degree is due to the PKP-triplications that occur at this distance. In Figure 4-2(b) there is a clear trend; $f_{\max}$ increases with increasing magnitudes. The value of $f_{\max}$ stays above 3 Hz for all distances and magnitudes. Consequently, this value should be sufficiently high to achieve a good resolution for the autocorrelations.

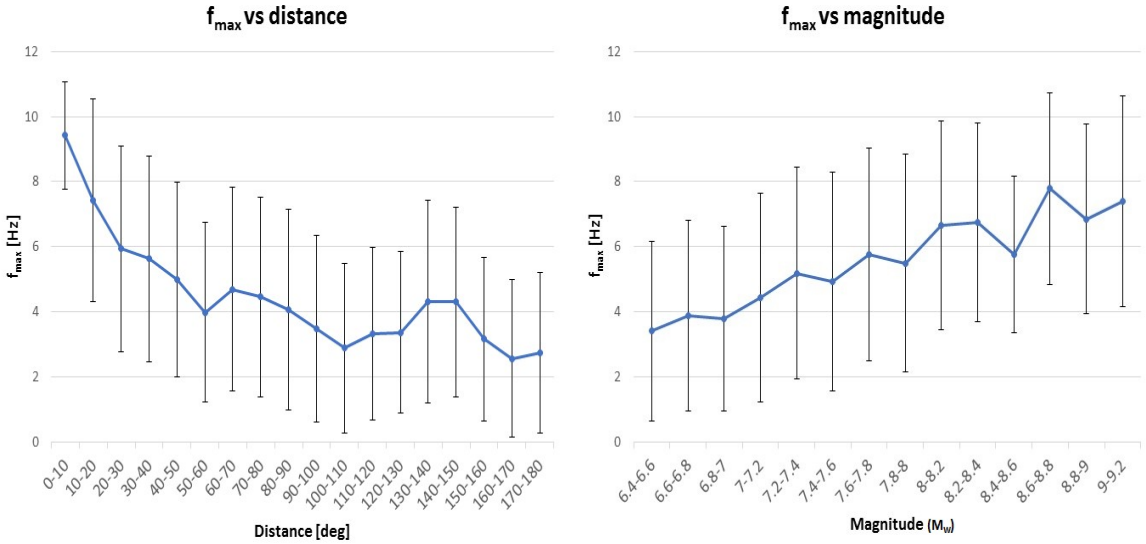

(a) $f_{\max}$ vs distance

(b) $f_{\max}$ vs magnitude

Figure 4-2: Maximum Frequency for different distances (left) and magnitudes in M_W (right), one side of the error bar is equal to 1 standard deviation.

Furthermore, it is also noted that the error bars, 1 standard deviation assuming Gaussian distribution, seem to be rather constant in both plots. However, it is expected that the error increases for higher magnitudes since less of these events occur, increasing the uncertainty of the measurements (e.g. magnitudes 6.4-6.6 include about 11000 station-event combinations, while for magnitudes 9-9.2 there are only 50). When further analyzing the data, it was found that there was a peak in events with a $f_{\max}$ histograms of 10 Hz, as shown in the histograms in Appendix A. These peaks are due to the implementation of the computation of $f_{\max}$, which looks for frequencies only between 0 and 10 Hz, and if no results are found in this range it sets $f_{\max}$ to a default of 10 Hz. This can happen due to either one of two reasons:

1. An erroneous measurement, which occurs for example when the FD SNR does not exceed the threshold of 5 dB for any of the frequencies between 0 to 10 Hz.

2. An event with $f_{\max}$ exceeding 10 Hz. Although no frequencies above 10 Hz were expected, it was found that especially the P- and PKIKP-phases sometimes go above this frequency (further on in Chapter 8, these specific events will be used for a high-frequency analysis).

Because it is impossible (without evaluating each event manually) to differentiate between these events, all these outliers have been removed for Figure 4-3. Unfortunately, the error still seems to be relatively constant, the histograms (Appendix A), however, show an improved distribution (closer resembling a normal distribution curve). It should also be noted that the average $f_{\max}$ is severely reduced by excluding the outliers, but the minimum value remains at 3 Hz, which, as stated before, should provide a fair resolution for the images.

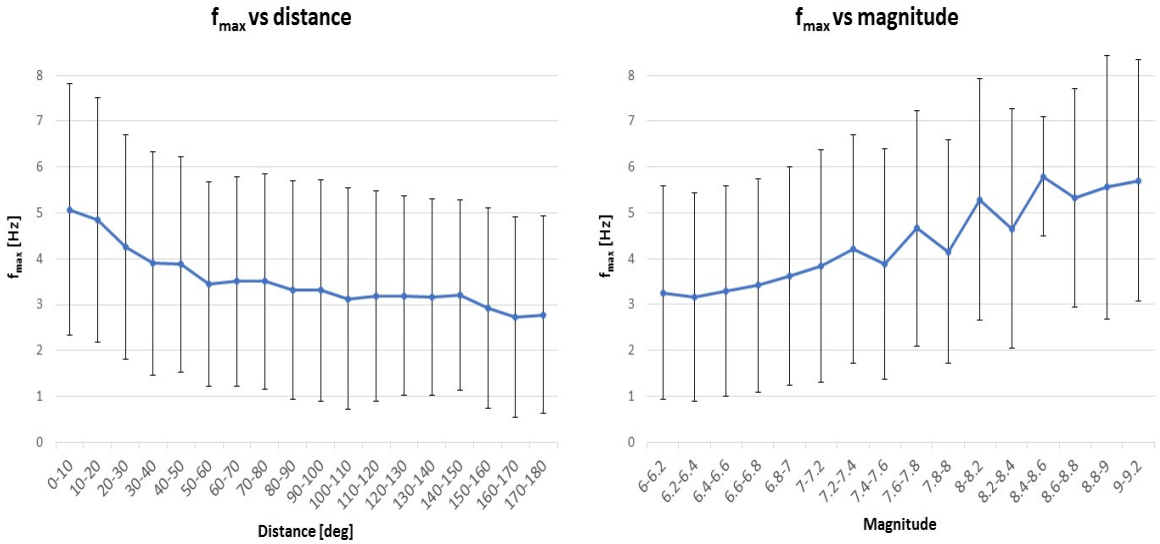

(a) $f_{\max}$ vs distance

(b) $f_{\max}$ vs magnitude

Figure 4-3: Maximum Frequency for different distances (left) and magnitudes (right), the error bars are equal to 1 standard deviation. Excluding the 9.9 Hz $f_{\max}$ outliers.

4-3 Fitting of the corner frequencies

Finally, the corner frequencies were fitted in order to compare the real spectra measured with theoretical spectra calculated as in Figure 3-5. In Figure 4-4 the average of f_c, based on magnitude increments of 0.1 M_W, is plotted against the amplitude (scaled by M_0). The size of the circles represent the amount of data, and since lower magnitude events are more likely to occur, the corresponding circles are bigger in size than the circles for higher magnitudes. Based on these weights the data is fitted using a linear least-squares fitting. To be able to do this linearly the common logarithm of both the frequency and amplitude is taken. Taking the logarithm also ensures that the residuals do not blow up at higher amplitudes, making the fit unbiased towards the logarithmic scale used in the Figure 4-4.

The fit is described by the following equation:

$$M_0 = 3 \cdot 10^{15} \ f_c^{-3.963} \tag{4-1}$$

According to Shearer (2009) M_0 depends on f_c as: $f_c \propto M_0^{-1/3}$, the fitted dependency of $-1/3.963$ is, therefore, slightly lower than the theory suggests. This means that the decay of f_c for our data is slightly lower than the theoretical decay. A possible reason for this difference is that the theoretical decay assumes self-similarity between earthquakes, which appears to be only roughly true for average earthquake properties. Moreover, very large earthquakes may rupture in a entirely different way compared to smaller earthquakes, which violates the self-similarity assumption (Shearer, 2009).
Finally, it should be noted that for high magnitudes there were only a few events available, introducing a large spread in these data. This means that the behavior of f_c for high magnitudes (greater than 8) is uncertain and might not be described well by the fitted formula.

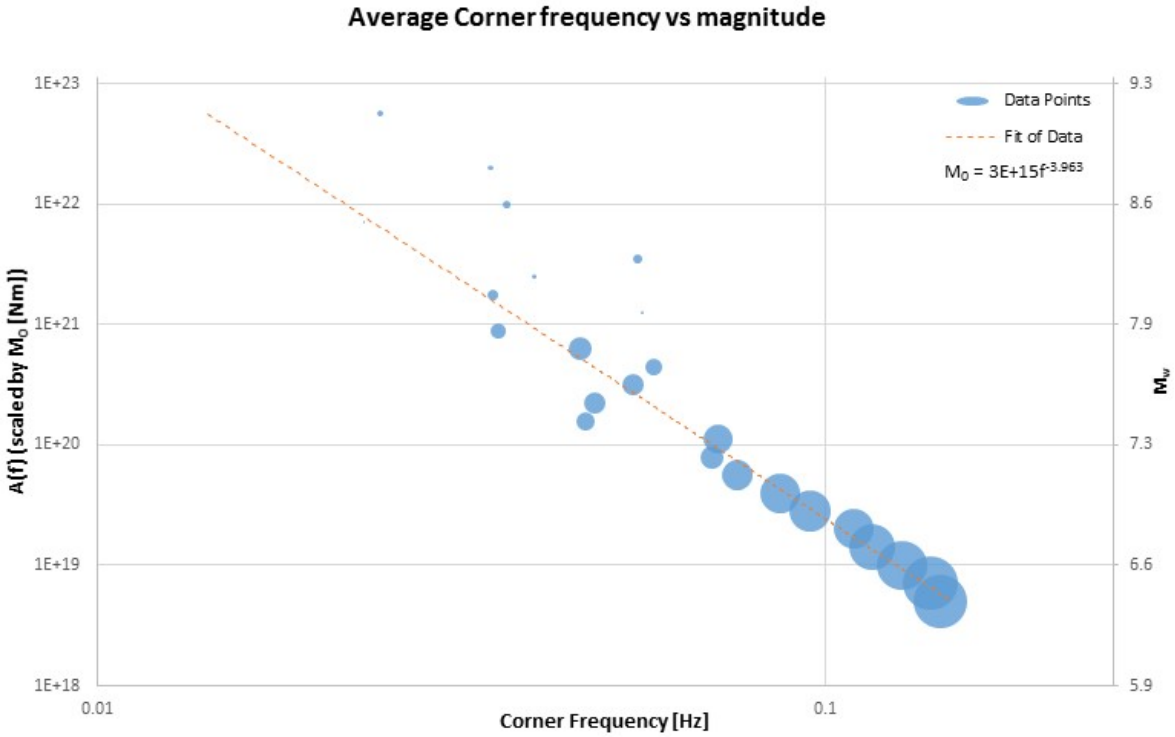

Figure 4-4: The calculated average corner frequencies for different magnitudes in blue are scaled by the amount of data they represent. The orange line is a fit through these points, using weighted linear least-squares fitting. The left axis is scaled by M_0, the right by M_W.

Chapter 5

Discussion and conclusions part 1

The analysis of this first part was done in order to find the ideal parameters for the application of seismic interferometry. The results of this first part will now be discussed. Starting with deriving suitable phases from the SNR graphs in Figure 4-1, followed by a discussion on $f_{\max}$ and f_c.
First, from the SNR results and the ray parameter (Figure 4-1 and Figure 3-4, respectively) a prediction of suitable phases in different distance ranges can be made:

- 0-75 deg: The ray parameters of most phases are too high, only PcP and PKiKP are sufficiently low to be viable options. However, the arrival of these phases overlaps with the arrival of either S-wave arrivals or surface waves, therefore, none of the phases is suitable for use at these distances.
- 75-100 deg: In this area, the P-phase arrival provides a high SNR, combined with sufficiently low ray parameter. Furthermore, the P-wave is the first to arrive and there is no overlap with the other phases, it is a good option for the autocorrelations.
- 100-120 deg: This range marks the start of the shadow zone, in the absence of P-wave arrivals it is found that the Pdiff-waves are the next best thing. However, because of their low SNR, they will most likely not give the best results.
- 120-140 deg: In this range, PKiKP-waves are a suitable candidate for retrieving zero-offset reflectivity estimates. Their ray parameter is favorably low, their SNR, on the contrary, is quite low and might be problematic.
- 140-180 deg: The peak in the SNR in this range seems quite promising, the only downside, however, is the overlap between the different phases. In this range, either PKP- or PKIKP-waves are suitable options.
- 165-180 deg: In this range PP-waves would be an option as well. However, these phases have traveled through the crust twice and are therefore more attenuated, viz. less likely to contain high frequencies.

Secondly, Figure 5-1 shows the expected amplitude spectral density based on the fitted corner frequencies (Figure 4-4) and the magnitude of the events. Equation 3-1 is slightly adapted, by

removing the site- and propagation-specific effects (which can only be done by also removing Ω_0, as these parameters were combined in the least-square fit). With the help of Equation 3-2 the magnitude of the event can be converted to M_0, which is used as an estimate for Ω_0, allowing for the expected spectra on the source-side to be estimated:

$$A(f)^{\text{scaled}}_{\text{source-side}} = \frac{M_0}{(1 + (f/f_c)^4)^{1/2}} \tag{5-1}$$

The resemblance of Figure 5-1 with the theoretical model by Madariaga (1976) in Figure 3-5 is clearly observed. Additionally, $f_{\max}$ is also displayed in the figure. For increasing magnitudes, $f_{\max}$ is also increasing, this means that ideally many high magnitude events are available since these events produce highest frequencies.

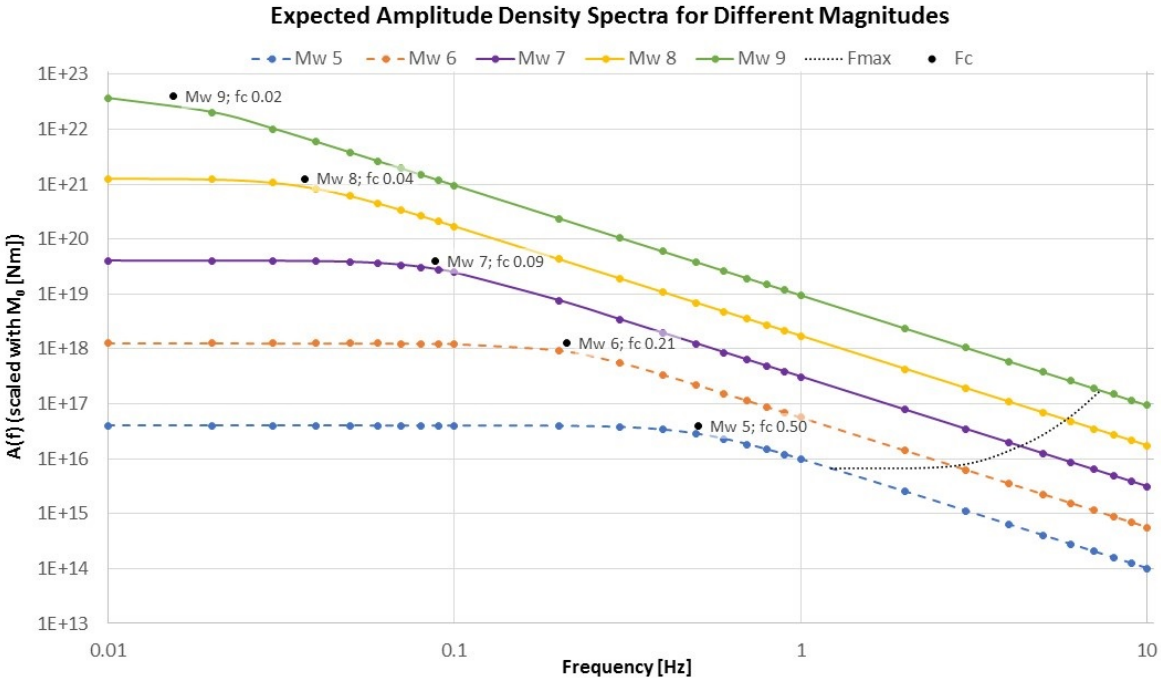

Figure 5-1: Expected source-side amplitude spectra (Equation 5-1) constructed based on the fitted corner frequencies (Figure 4-4), and M_0 calculated from the magnitudes (Equation 3-2). The dashed colored lines indicate that f_c was extrapolated from the data, while the solid colored lines are within the same range as the original data. Finally, $f_{\max}$ is also included (black dotted line) based on Figure 4-2(b).

Although the results indicate that the very high maximum frequencies up to 8 Hz, shown by Verdel et al. (2016), are less common, the lowest value of 3 Hz is still considerably higher than the value of 1 or 1.5 Hz, that other methods have used so far. Furthermore, it was seen that there are a number of very high frequency events in the data as well, albeit that these events are relatively rare.
In the second part, three case-studies will be considered, in order to evaluate if the method is actually capable of retrieving high frequency structural information, as the results from the first part seem to suggest.

Part II

Case studies

Chapter 6

Malargüe, Argentina

Based on the results of the first part, a large number of events containing sufficient energy at high frequencies are expected to occur, which can be used for application of GloPSI HF. In this second part, three case-studies will be considered to evaluate whether there is actual structural information in these events. First, the Malargüe T-array in Argentina will be considered (Ruigrok et al., 2012). This array is located east of the Andean Mountain range as shown in Figure 6-1. The array consists of 32 short-period (with a corner frequency of 2 Hz) stations, which were active during 2012 (Weemstra et al., 2017).

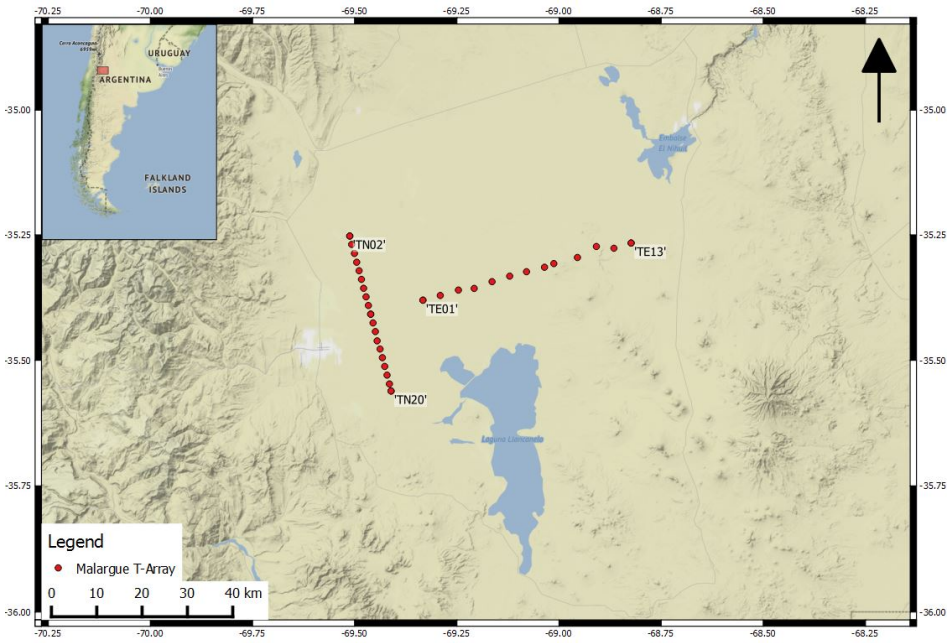

Figure 6-1: Location of the Malargue TE- and TN-array stations (red), the first and last stations of the lines are labeled with the station code. The inset shows the location in Argentina (red box). Map tiles by Stamen Design (2011), under CC BY 3.0. Data by OpenStreetMap contributors (2004), under ODbL.

6-1 Geological setting

The array is located approximately 10 km east of the fold axis of the north-south Malargüe anticline (Kraemer et al., 2011), which means it is on top of the sedimentary syntectonic structure, known as the Malargüe basin (Weemstra et al., 2017). The north-south line (stations with the prefix "TN") is located in parallel to the anticline axis, therefore the basin depth is expected to be approximately constant along the stations. The stations along the east-west line (prefix "TE") are perpendicular to the basin, meaning that the sediment thickness is decreasing from west to east. Nishitsuji et al. (2014) also found this by applying global phase H/V spectral ratio (GloPHV) to the data from the Malargüe array, as shown in Figure 6-2. The GloPHV is a technique that takes the amplitude spectral ratio between the horizontal (H) and vertical (V) components of global phases, to estimate the local S-wave resonance spectrum, which gives an indication of the thickness of a geological layer, in our case: the basin thickness (Nishitsuji et al., 2014). In Figure 6-2b a clear dipping structure is observed, indicating that the upper sedimentary layer is thinning towards the east.

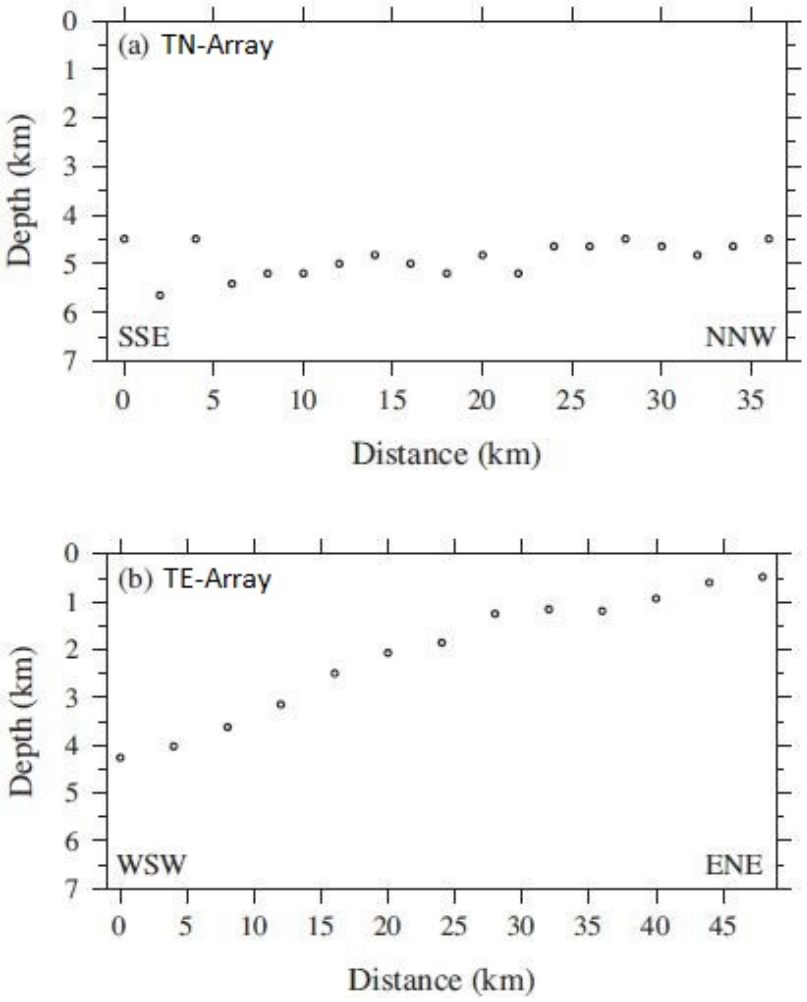

Figure 6-2: The basin depth below the TN- and TE-array (top and bottom, respectively) estimated by fundamental resonant periods. Results from Nishitsuji et al. (2014).

6-2 Methods

The data acquisition is similar as for the USArray (see Figure 3-1): again the recordings and events are extracted from the IRIS database after which the $f_{\max}$ and other parameters are computed and stored. Once more, only earthquakes with magnitude greater than 6.0 were selected.
From the database a first pre-selection is made by considering only a certain seismic phase and a small angle of incidence ($\leq 15^o$). The angle of incidence is determined using the ray parameter (s/km) and the velocity of 5.8 km/s for the upper layer of the IASP91 model (Kennett and Engdahl, 1991):

$$\alpha = \arcsin(5.8p) \tag{6-1}$$

Where α is the angle of incidence in degrees and p the ray parameter in s/km. The small angle of incidence ensures that the retrieved reflection estimates can be considered as zero-offset. Furthermore, it is ensured that the fitting function succeeded in finding the $f_{\max}$ (Section 3-2), meaning that events, where the function failed (i.e. where the computation of $f_{\max}$ defaulted to 10 Hz), are discarded.
Next, for each station a number of n events with the highest $f_{\max}$ are selected, where n is the desired number of events for a stack. The number of stacks can either be set to a fixed number or to the number of events with $f_{\max}$ greater than a threshold (both cases will be studied later). After deconvolving the waveform data with the instrument response, 2 minutes of the phase response of the event is cut from the data. Optionally, the amplitude spectra are whitened afterwards. Spectral whitening is a technique that aims to equalize the amplitude spectrum. In our case, spectral whitening is applied in a sliding window with a narrow frequency band, in which the spectrum is normalized. The final step before autocorrelation is band-pass filtering the data: the upper cutoff frequency is set to $f_{\max}$ and the lower cutoff frequency is set empirically, but such that the filter pass band contains at least one octave. Next, the autocorrelation is computed and the signal is normalized by the maximum amplitude, before stacking all the events together. This process is then repeated for the other stations, after which the stacks are plotted together to form one 2D section. This whole process is shown schematically in Figure 6-3.

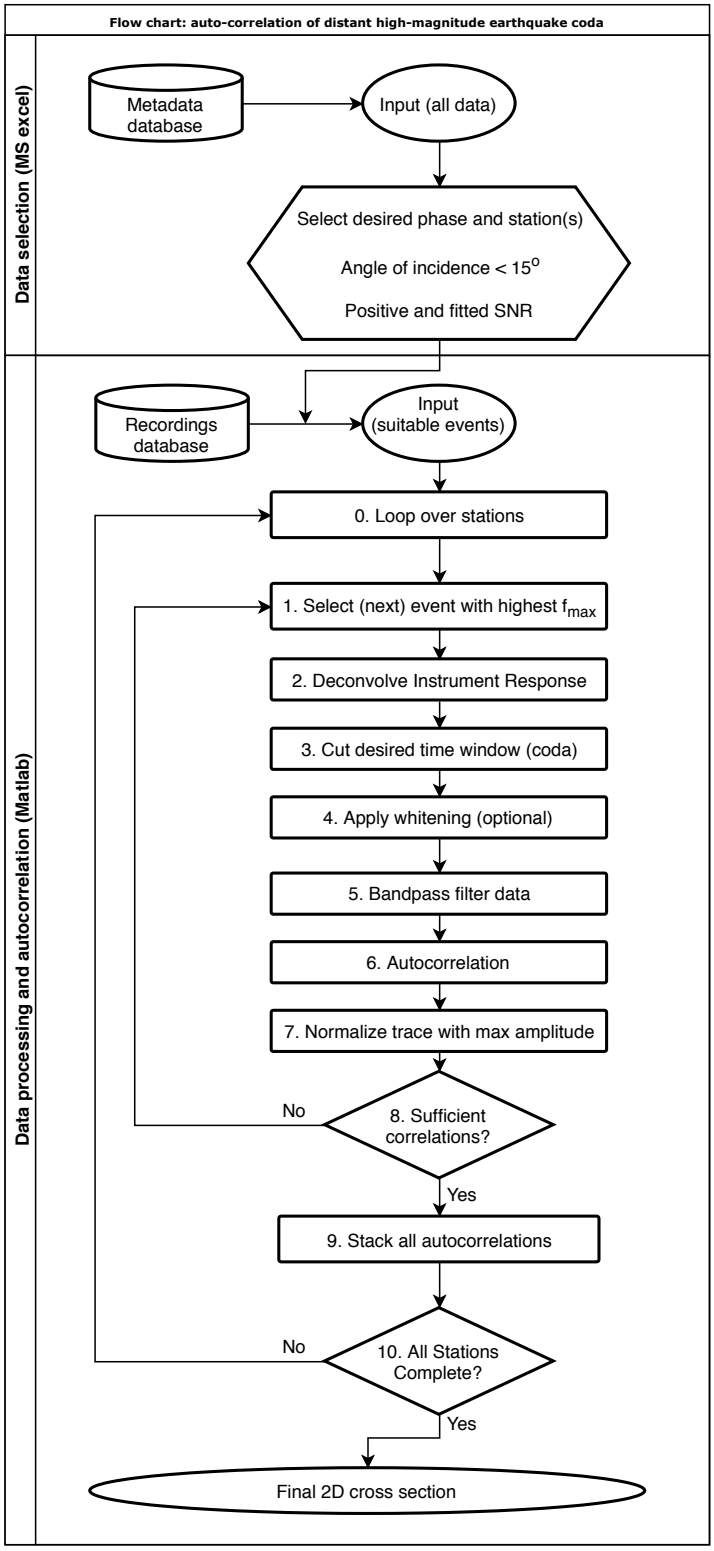

Figure 6-3: Flowchart showing the process for the autocorrelation of distant earthquake coda (adaptation for GloPSI HF from Draganov and Ruigrok (2014)).

6-3 Selected events

As explained in the methodology (Figure 6-3) the first step is to select suitable events. The number of selected P-phase events is very low (8 unique events, but not recorded by all stations), therefore it is decided to not compute P-phase correlations. Instead PKIKP-events are considered. In Figure 6-4 the origin of these events is shown. Please note that the size of the circles, in this case, does not show the magnitude of the event, but rather the number of stations that used the particular event for its autocorrelation stack (large circles mean that more stations included that event in their stack).

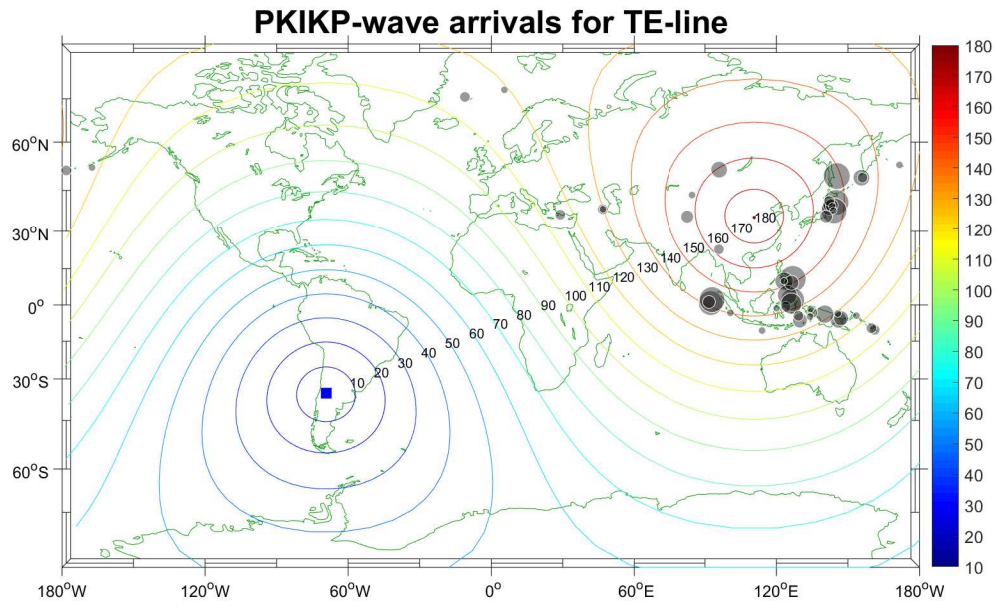

Figure 6-4: PKIKP-events used for stacking. The size of the circles represents the number of stations that use that particular event, NOT the magnitude (bigger circles means the event is used by more stations). The blue square represents the center of the Malargüe T-array, the colored lines represent the isolines of distance (in degrees) from this center. Map created with the M_Map package (Pawlowicz, 2000).

In the case of the Malargüe array, it is decided to stack 10 events, because more stacks would require the maximum frequency to be lowered to a value deemed too low to retrieve high-resolution subsurface reflectivity, whereas fewer events would decrease the reliability of the data. For consistency each station uses the same, fixed number of 10 stacks, even though some stations still allowed for extra events to be stacked based on their individual $f_{\max}$ value. This can be seen in Table 6-1.
In Table 6-1 the $f_{\max}$ of the last event added to the stack is noted, this means that this is the event with the lowest $f_{\max}$ in the stack (since the highest $f_{\max}$ events are selected first). An interesting thing that can be noted in the table is how $f_{\max}$ increases away from station TE01, which means that $f_{\max}$ increases towards the east or, equivalently, with decreasing basin depth. This increase with station number is in line with the increase of the (H/V) resonant frequency with station number (Nishitsuji et al., 2014). The total available number

of events displays a similar trend, although less pronounced. This is a first indication for the dip in the basin because a thicker sediment layer will lead to more attenuation of the waves and therewith decrease the maximum frequency. Therefore the slope in figure 6-2b seems to manifest itself in the data here as well. The results in the next section will confirm this observation.

Table 6-1: Table showing for each station how many events from the total number of events are used in the stack (i.e. the stacking-fold), as well as displaying the lowest f_{max} of all the stacked events (minimum f_{max}).

Stations	Stack/Total	f_{max} [Hz]
TE01	10/35	2.61
TE02	10/40	3.09
TE03	10/33	2.52
TE04	10/45	2.76
TE05	10/50	2.93
TE06	10/48	3.82
TE07	10/55	3.84
TE08	10/47	4.85
TE09	10/51	7.51
TE10	10/52	3.98
TE11	10/53	5.81
TE12	10/38	4.28
TE13	10/46	5.43

Finally, based on Table 6-1 it is decided to set the high cut-off of the filter to 3 Hz. This is a compromise, which does include a little noise in the stack of some stations, but since this is only the case for a few events, there should still be sufficient signal. Moreover, this ensures that the results use most of the high frequency signal available in the data.

6-4 Results

In accordance with Equation 2-2 an autocorrelation is negated to obtain an estimate of the reflection response below the stations. The final results for the TE-line are shown in Figure 6-5, the color map in these figures ranges from negative amplitudes (red) to zero (white) to positive amplitudes (blue). Figure 6-5(a) shows the results without whitening and 6-5(b) does have whitening applied. The two-way travel time is converted to depth using a velocity of 5.2 m/s taken from a study by Farías et al. (2010). Taking the same velocity everywhere is a rather crude way of converting to depth, but it does allow a better comparison with Figure 6-2. The non-whitened result (6-5(b)) uses a 4th-order Butterworth filter between 1.25 and 3 Hz. By spectral whitening a more constant spectrum is obtained, allowing more lower frequencies to be included (these frequencies would be dominating without whitening as they have the highest amplitude). The whitened result (6-5(a)) therefore uses a 4th-order filter between 0.6 and 3 Hz.
From Figure 6-5 the depth of the basin can be estimated as well, for this consider the final strong blue reflector, starting at about 4 km depth on the left in the figures. The basin

structure can also clearly be observed in the results, with the structure and depth closely resembling the result in Figure 6-2(b). Furthermore, a dim spot can be noted below stations TE02 to TE05. This spot is explained by the higher attenuation of the waves in the sedimentary basin. Finally in a similar manner as described before the TN-line is also processed. The results, shown in Figure 6-6 may not be as spectacular as the TE-line as no definite basin depth can be identified. However, the clear horizontal structure shown in the figure is agreeing with Figure 6-2(a). Moreover, in Figure 6-6(b), there does seem to be a slightly stronger blue reflector at a depth of about 4 to 5 km, the expected depth according to figure 6-2(a). This reflector has the same polarity as the results of the TE-line, therefore it is likely the bottom of the basin. However, this reflector is not as continuous as the reflector of the TE-line, making it harder to observe the bottom of the basin here.

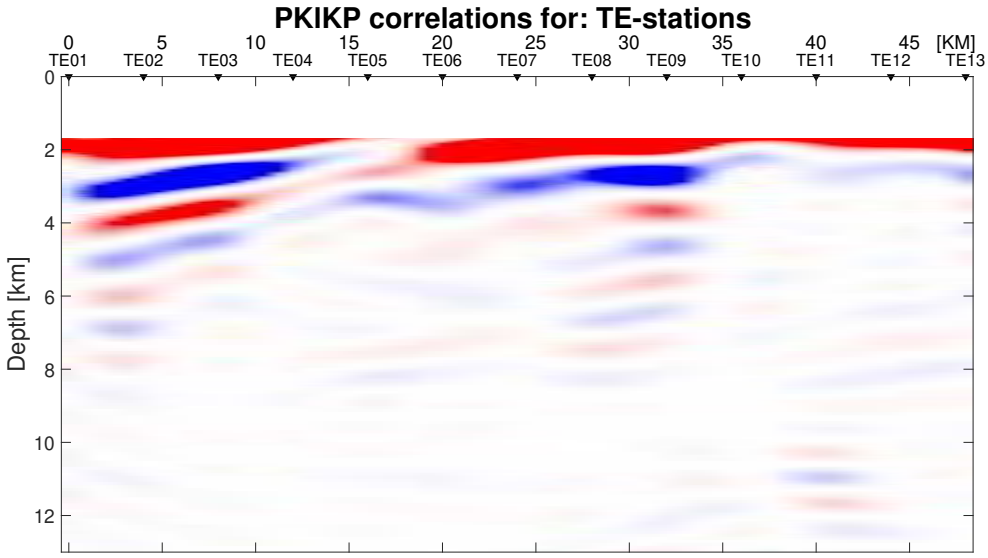

(a) TE without whitening

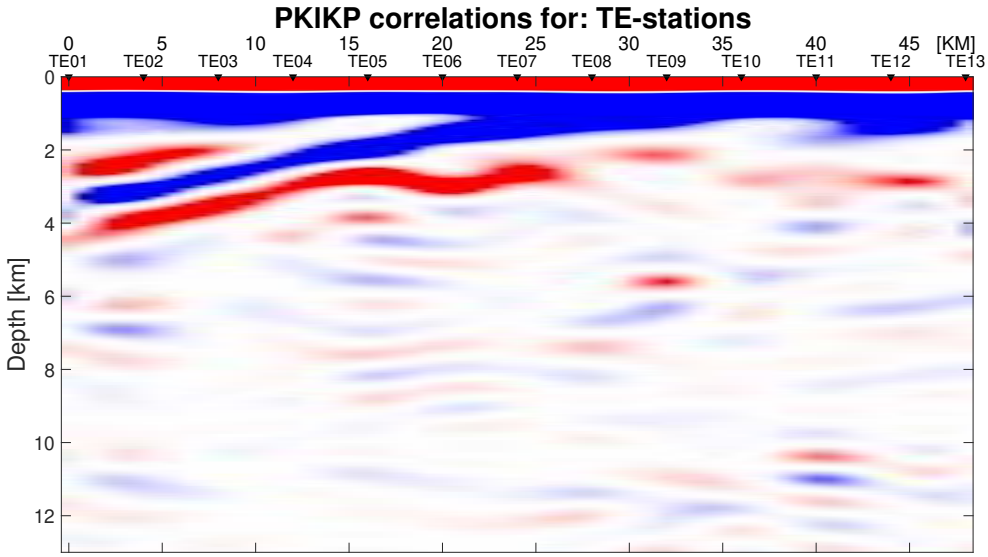

(b) TE with whitening

Figure 6-5: Result for the TE-line using a 10-fold stack of PKIKP events, using a 4th-order Butterworth filter between 1.25 and 3 Hz for the image without whitening and a 4th-order Butterworth filter between 0.6 and 3 Hz for the whitened image. In the top figure the first 0.65 seconds have muted, to highlight the lower part of the image.

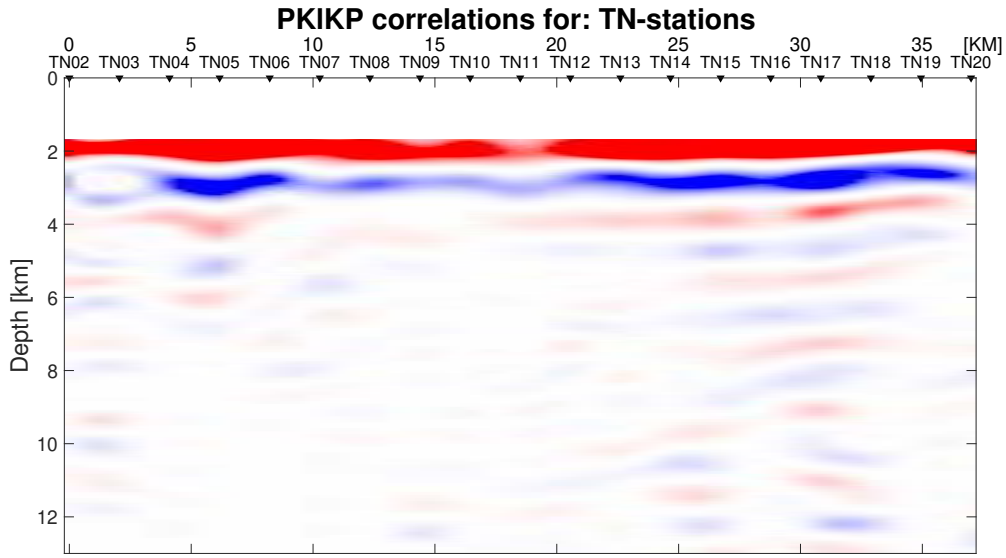

(a) TN without whitening

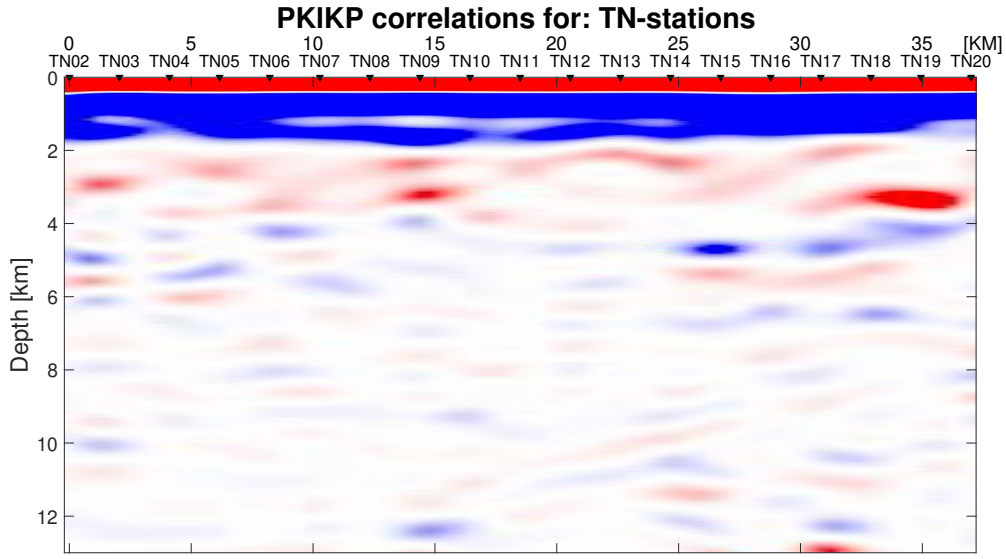

(b) TN with whitening

Figure 6-6: Result for the TN-line using a 10-fold stack of PKIKP events, using a 4th-order Butterworth filter between 1.25 and 3 Hz for the image without whitening and a 4th-order Butterworth filter between 0.6 and 3 Hz for the whitened image. In the top figure the first 0.65 seconds have been cut from the window.

ANSI

For comparison, an ANSI study is also attempted on the data. This is done by stacking of autocorrelations for the entirety of 2012, with a time window of 10 minutes and an overlap of 5 minutes between the correlations. Figure 6-7 shows the ANSI results per month. This result is achieved without any filtering of the data because it is found that any filter applied to the data would cause ringing artifacts. A possible explanation for these artifacts is the spiky nature of the diurnal recordings, as observed by Weemstra et al. (2017). Of course, the unfiltered data cannot be compared with the GloPSI HF results, since the frequency content of both results is completely different. Still, Figure 6-7 displays some interesting results; especially in January, February and December a wedge structure can be observed. Note that this structure is located at about 6 seconds of TWT, whereas the basin depth found in the GloPSI HF study is found at approximately 1.5 seconds TWT ($\sim$ 4 km). However, it is likely that the structure is continued at greater depths below the sedimentary basin. This statement is also confirmed by Nishitsuji et al. (2016), who found a wedge feature at an even greater depth of 12.5 seconds TWT.
Even though a full year of data was used, during this year the stations can be inactive for periods of time. For example, station TE12 did not record any data in the months November and December, and station TE03 was mostly inactive in August and September. Consequently, the data quality and coverage is not necessarily the same for each month. The full availability of the data is listed in Weemstra et al. (2017).

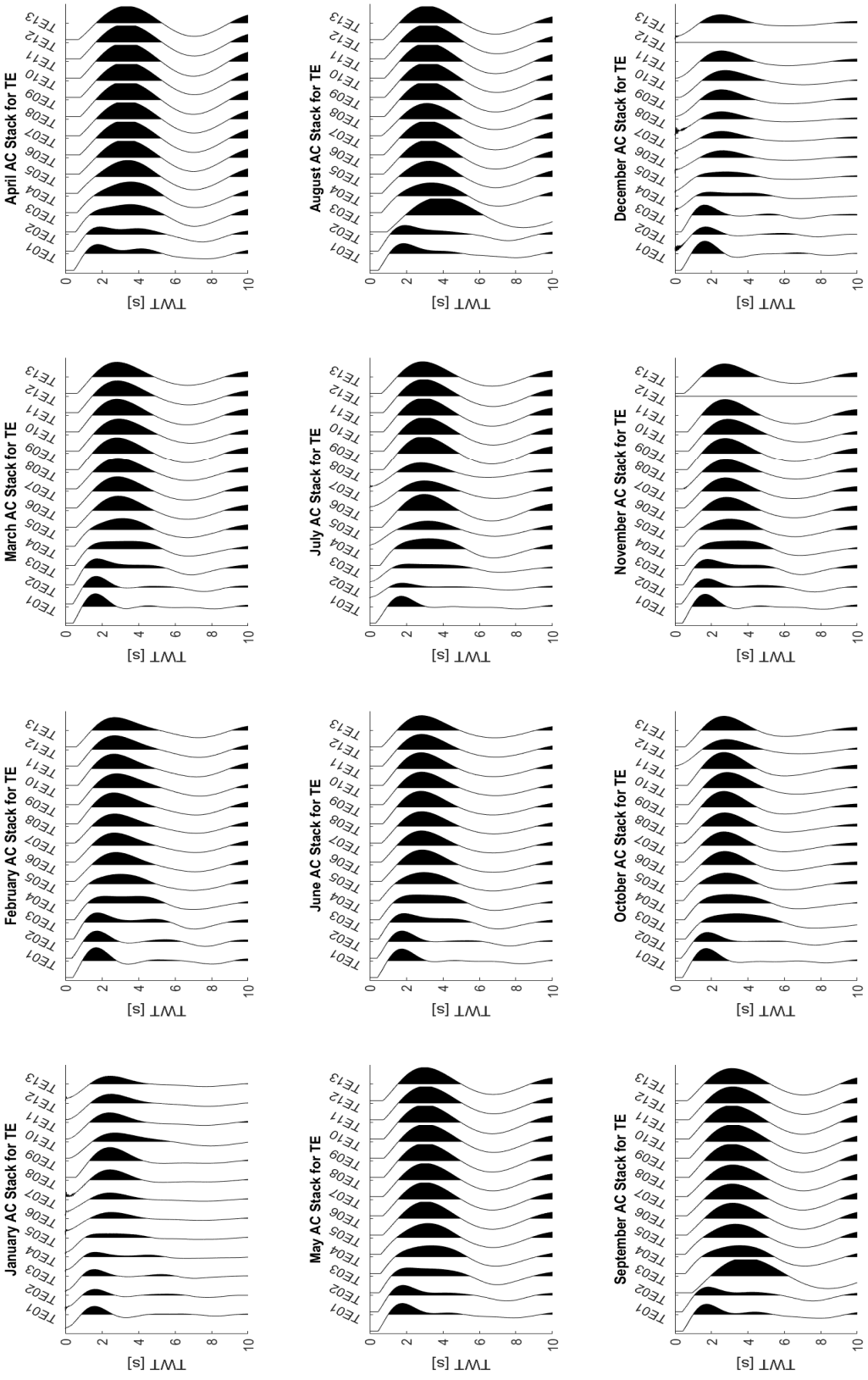

Figure 6-7: ANSI results per month of the TE-line, no filter has been applied to the data.

Chapter 7

SPREE array, US

The second case study concerns the use of the SPREE array, located in Minnesota and Wisconsin, USA (and some stations in Canada which will not be considered now). The array was designed to get a better understanding of the Mid-Continent Rift (MCR) (Stein et al., 2011). In total, 67 broadband stations, divided over 3 lines (SN in the north, SM in the middle and SS in the south), were deployed from 2011 to 2013, as shown in Figure 7-1. For this study specifically the SN-line (stations SN43 to SN63), from north-west to south-east, will be considered.

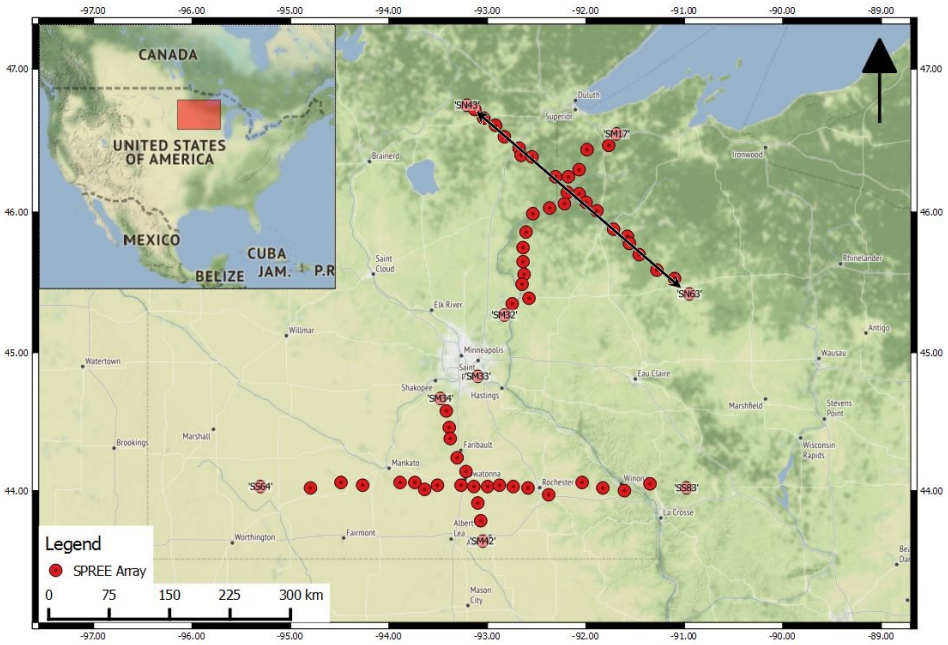

Figure 7-1: Location of the SPREE-array stations (red), the station codes are shown for a few stations, the extend of the SN-line is marked with the double line arrow. Inset shows the location within the United States (red box). Map tiles by Stamen Design (2011), under CC BY 3.0. Data by OpenStreetMap contributors (2004), under ODbL.

7-1 Geological setting

The exact structure below the SPREE-array is unknown. However, there have been studies in the area giving an indication of what to expect. Figure 7-2 shows the Bouguer anomaly in the area, the MCR is clearly observed as a positive gravity anomaly (Stein et al., 2011). The SN-line is perpendicular to this anomaly, meaning that the rift is expected to be observed in this cross-section. An active seismic reflection survey was conducted over Lake Superior, about 100-200 km from the SN-line (see Figure 7-2), also situated perpendicular to the MCR Green et al. (1989). Even though this project, called GLIMPCE (Great Lakes International Multidisciplinary Program on Crustal Evolution), is quite far from our survey, it can still provide some valuable insights on the possible structure of the MCR. Stein et al. (2016) adapted the original seismic results in a cross-section of the rift, which is shown in Figure 7-3 and concluded that the MCR is a sequence of alternating half-grabens. In this section, a basin can be observed that is thick in the middle and thinning towards the sides. The thick middle of the section is likely the cause of the gravity anomaly in Figure 7-2. Based on these observations, a similar structure is expected for the SN-line, with layers on both sides dipping towards the middle.

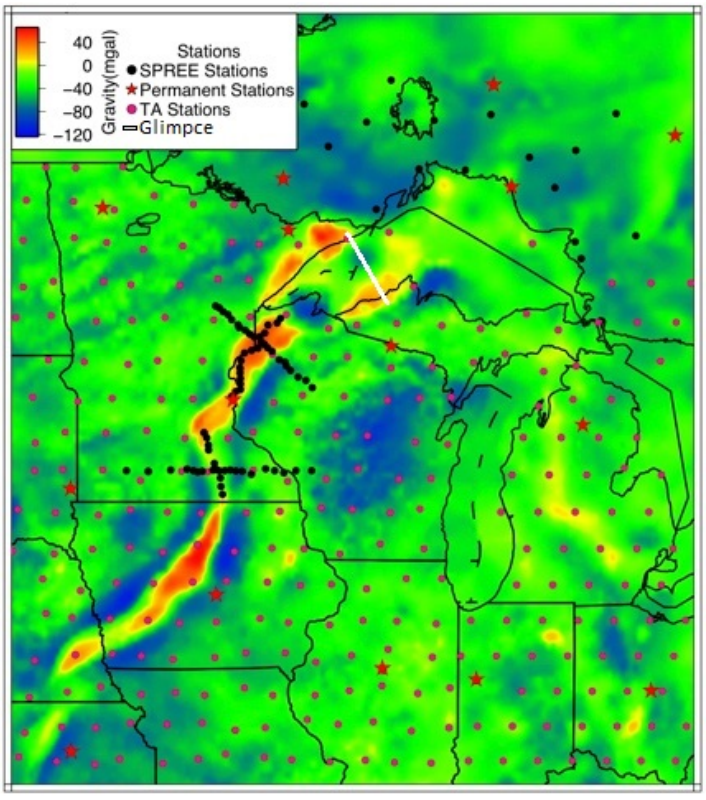

Figure 7-2: Map showing the Bouguer Anomaly below Minnesota. The black dots represent the SPREE array, the white line shows the location of the GLIMPCE experiment. Adapted from Stein et al. (2011).

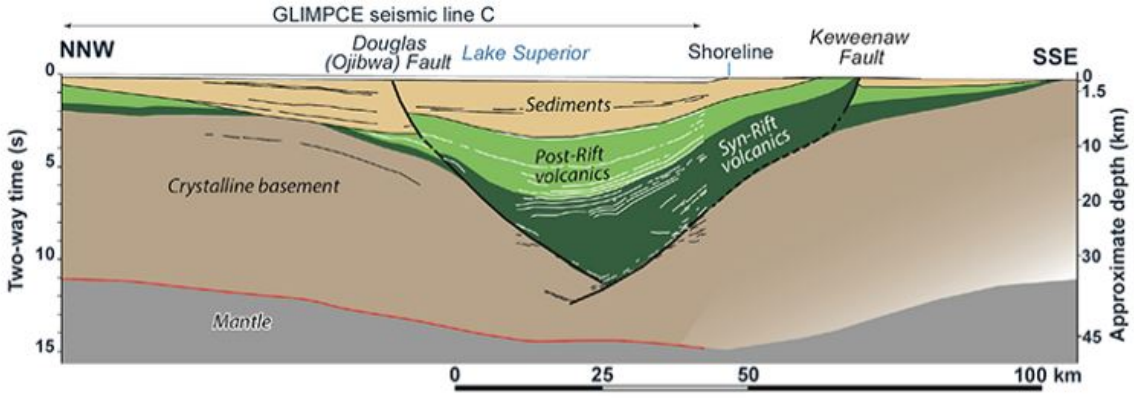

Figure 7-3: Interpreted cross-section from the GLIMPCE survey, by Stein et al. (2011).

Shen et al. (2016) found this dipping trend towards the middle of the SN-array by calculating the Receiver Function below the stations, as shown in Figure 7-4. Note that receiver function time is one-way time, so these values need to be doubled to get TWT and compare the results with GloPSI HF. Using this method the Moho beneath the station is very well imaged. However, the resolution in the upper crust is quite low and no distinct features can be recognized. In this chapter GloPSI HF will be used to get a higher resolution image of the upper crust below the SN-line.

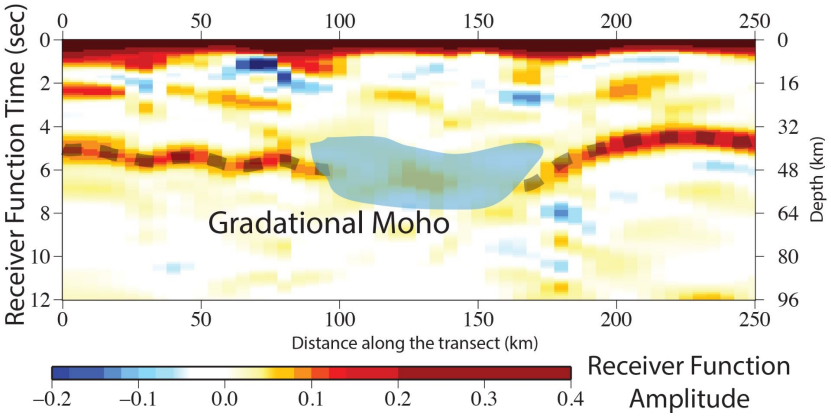

Figure 7-4: Images of the receiver function below the SPREE SN-line (starting with station SN43 at the left) adapted from Shen et al. (2016).

7-2 Selected events

The SPREE-array is located optimally for P-phases, as there are many P-events with a good azimuthal spread, as is shown in Figure 7-5. The large azimuthal spread is beneficial for a number of reasons. First, it limits the source-side effects, ensuring that the observed results are indeed receiver-side reflection responses. Furthermore, the azimuthal spread ensures illumination from different angles, which is especially desired for P-phase events with relatively large angles of incidence. The PKIKP events (Figure 7-6) mostly originate from Indonesia,

at a distance of 120 to 140 degrees. Once again note that the size of the circles in these figures represents the number of stations using that specific event, and are unrelated to the magnitude.

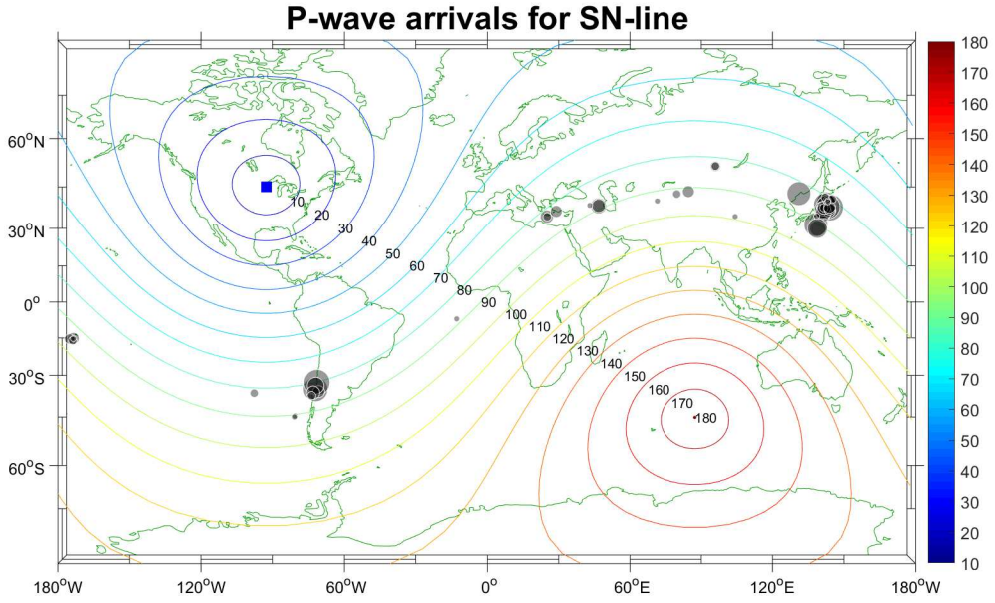

Figure 7-5: P-events used for stacking. The size of the circles represents the number of stations that use that particular event, NOT the magnitude (bigger circles means the event is used by more stations). The blue square represents the center of the SPREE array, the colored lines represent the isolines of distance (in degrees) from this center. Map created with the M_Map package (Pawlowicz, 2000).

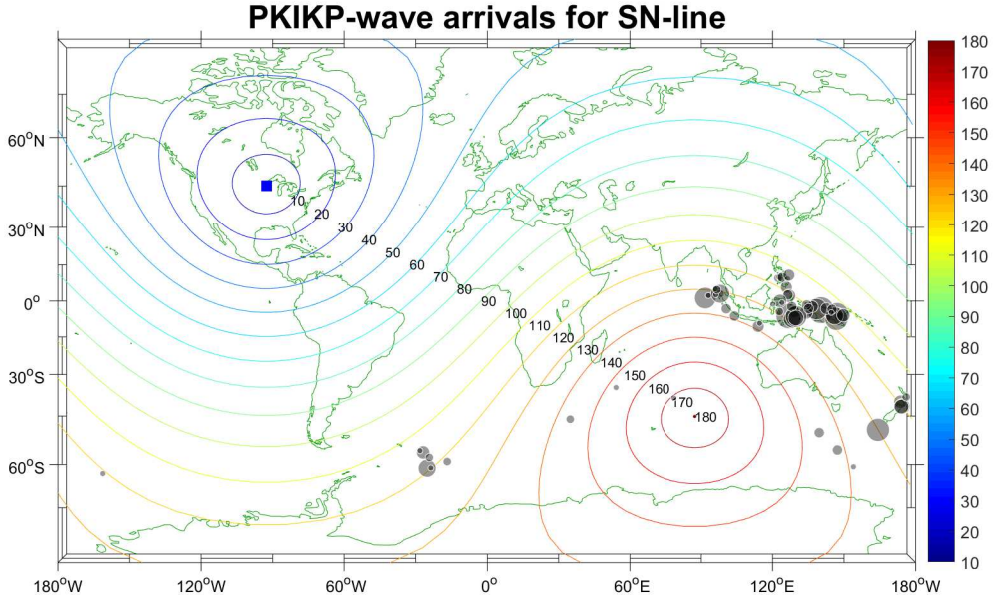

Figure 7-6: PKIKP-events used for stacking. The size of the circles represents the number of stations that use that particular event, NOT the magnitude (bigger circles means the event is used by more stations). The blue square represents the center of the SPREE array, the colored lines represent the isolines of distance (in degrees) from this center. Map created with the M_Map package (Pawlowicz, 2000).

The processing is done similarly to the Malargüe array, again the flowchart in Figure 6-3 was followed. However, there are more high frequency events allowing the use of 15 events per stack. Again the maximum frequency is set to 3 Hz, based on the values in Table 7-1. This time there are no particular trends found in the maximum frequency values, and also the number of total events is relatively consistent for all stations. Finally, the differences between the P and PKIKP events are quite small, but generally, PKIKP has a slightly higher $f_{\max}$ (with the exception of the first 3 stations). Finally, the filter settings were adapted for the SPREE-array as well, this is explained in the next section, which also presents the final results.

Table 7-1: Table showing for each station how many events from the total number of events are used in the stack, as well as displaying the lowest $f_{\max}$ of all the stacked events (minimum $f_{\max}$). On the left the P-phase and on the right the PKIKP-phase events are displayed.

	P		PKIKP	
Stations	Stack/Total	$f_{\max}$ [Hz]	Stack/Total	$f_{\max}$ [Hz]
SN43	15/39	3.27	15/25	2.91
SN44	15/46	4.94	15/33	3.75
SN45	15/36	2.93	15/29	2.78
SN46	15/45	3.72	15/36	3.81
SN47	15/41	4.91	15/38	6.01
SN48	15/41	2.60	15/40	2.62
SN49	15/37	3.26	15/41	3.79
SN50	15/30	2.84	15/35	4.64
SN52	15/48	4.62	15/40	5.32
SN53	15/37	3.52	15/44	4.48
SN54	15/41	2.77	15/37	3.14
SN55	15/41	3.08	15/37	3.44
SN56	15/40	3.39	15/36	4.01
SN57	15/42	3.37	15/41	4.68
SN58	15/37	3.32	15/39	3.52
SN59	15/40	3.13	15/44	4.35
SN60	15/38	3.32	15/43	4.34
SN61	15/42	4.39	15/43	6.76
SN62	15/34	2.68	15/30	3.30
SN63	15/41	3.96	15/45	5.19

7-3 Results

The final results for the individual P and PKIKP sections are shown in Figure 7-7 (no whitening) and Figure 7-8 (whitened). Again, the color map in these figures ranges from negative amplitudes (red) to zero (white) to positive amplitudes (blue). Please note that the stations are in reality not evenly distributed along the 230 km line (as shown in Figure 7-1), even though they are plotted with equal distances in the figures. The gravity anomaly (Figure 7-2) is strongest below station SN53, which is slightly left of the middle section.

As stated before, the filter settings are adapted for the SPREE-array, instead of using a 4th-order Butterworth filter, a filter with an order of 5 on the low-frequency side and an order of 3 on the high-frequency side is chosen. In the case of a Butterworth filter the order determines how steep the amplitude drop is on the edges: a higher order means a steeper slope, while low order has a more gentle slope. For SPREE specifically, the filter has a steep cut-off on the low-frequency side in order to exclude low frequencies. On the high-frequency side on the other hand the filter is more gentle, allowing more high-frequency data to be included. This does mean that not only more high frequency signal is added, but also more noise is allowed. For the whitened result the low-frequency cut-off is not necessary since the spectrum has been equalized. The whitened data, therefore, uses a 4th-order bandpass filter in the 1 to 3 Hz band.

A number of observations can be made from the final results. First, the similarity between the P and PKIKP sections, for example, refer to the feature seen at around 0.5 seconds below station SN49 in the non-whitened result (in the whitened result it is a little less apparent but still visible). Secondly, there is a dim spot right in the middle of the section, this could be hinting towards a thicker layer of sediments in this array (as seen in the Malargüe results). Lastly, there seems to be a slight hint of a dipping trend from the sides to the middle, this can especially be seen in the PKIKP sections (7-7(b) and 7-8(b)).

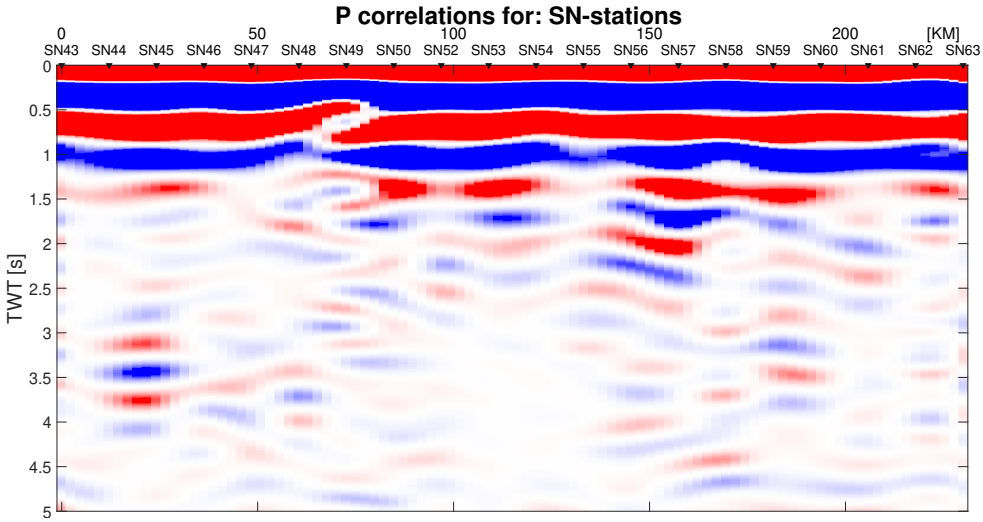

(a) SN-line P events

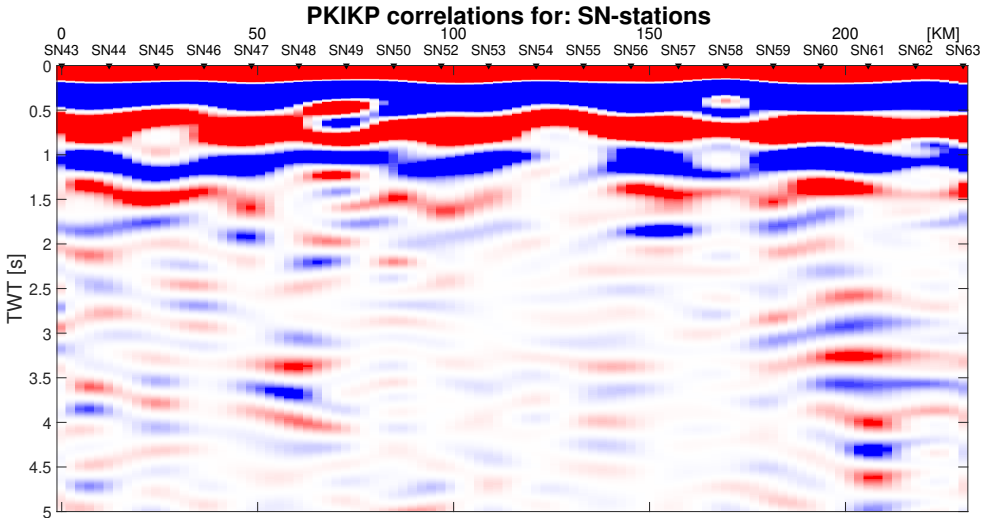

(b) SN-line PKIKP events

Figure 7-7: Result for the SN-line using a 15-fold stack of P (top) or PKIKP (bottom) events, using a Butterworth filter between 1.25 and 3 Hz, with an order of 5 at the low frequency side and an order of 3 at the high frequency side. No whitening has been applied.

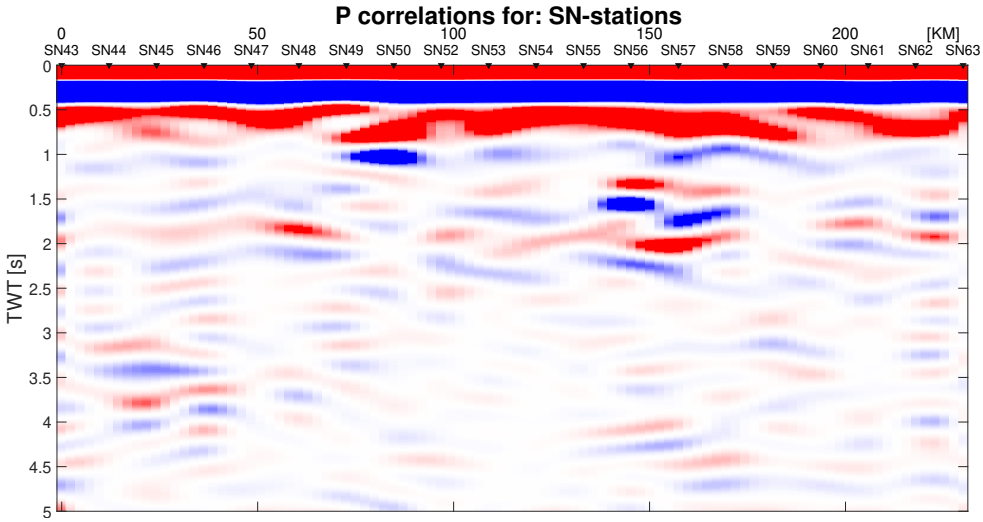

(a) SN-line P events

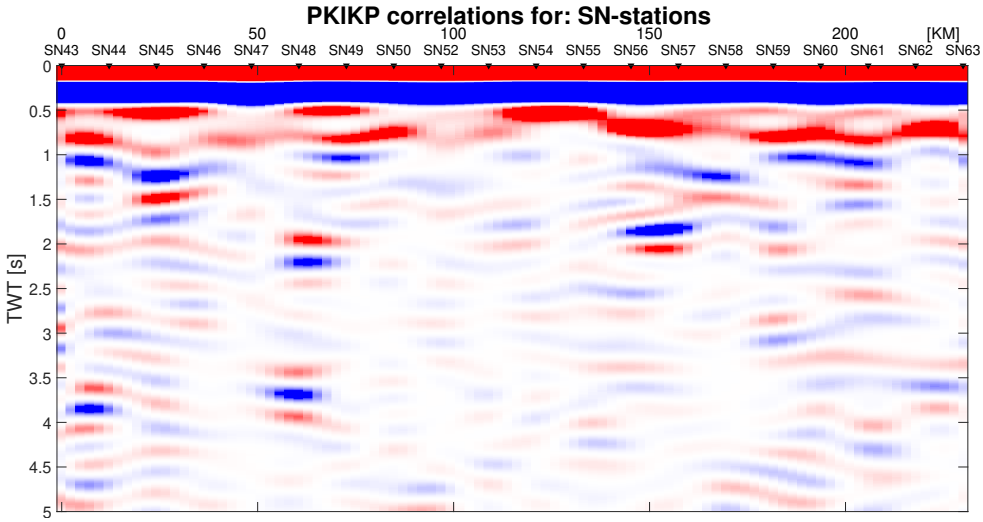

(b) SN-line PKIKP events

Figure 7-8: Result for the SN-line using a 15-fold stack of P (top) or PKIKP (bottom) events, using a 4th-order Butterworth filter between 1 and 3 Hz. Whitening has been applied.

Combined P and PKIKP result

As discussed before, solely using P-phases will result in an illumination gap for the low ray parameters ($\leq$ 0.04 s/km). Therefore, a combined section containing both P and PKIKP events is also made (this also allows for a stack of 30 events in total). This will increase the total signal in the cross-section and more noise will be stacked out of the section. Figure 7-9 shows the results of using both phases, also in this figure the first 0.5 seconds are muted to better display the deeper part of the section. The remainder of the processing has been done in the same manner as with the original whitening results.

In the figure, one can observe a structure (highlighted with black dots) closely resembling a basin in the center of the image (starting at $\sim$ 40 km to $\sim$ 150 km). The depth of about 2 seconds TWT is close to the thickness of the sedimentary layer in Figure 7-3, suggesting that it is indeed a sedimentary basin that is imaged. Moreover, the location of this basin structure also coincides with the location of negative receiver function amplitude, also found in the 50 to 150 km range, shown in Figure 7-4. The structure is then repeated at about double the TWT, this could be a multiple of the original structure. However, it could also be an actual feature, as the syncline structure is also expected at larger depths, as discussed before in the geology section.

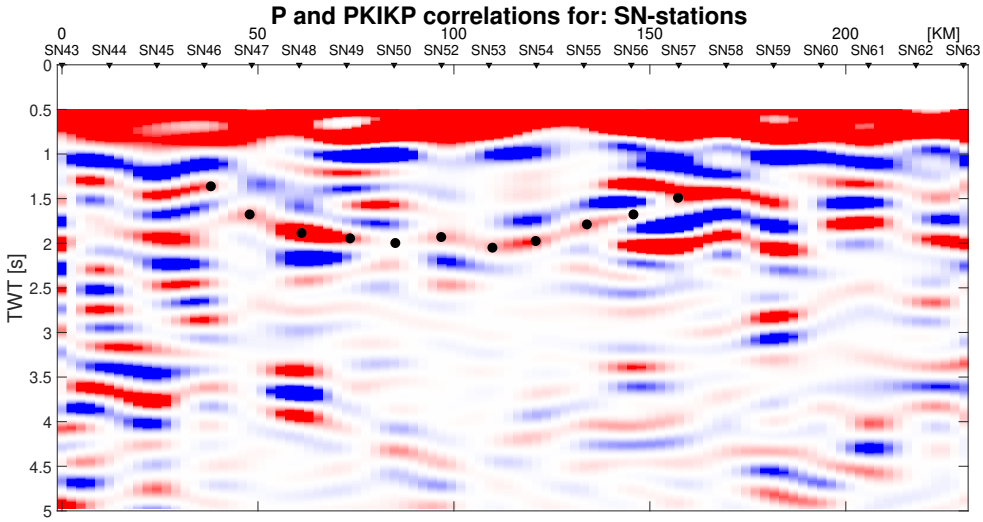

Figure 7-9: Result for the SN-line using a 30-stack fold of combined P and PKIKP events, using a 4th-order Butterworth filter between 1 and 3 Hz. Whitening has been applied. The black dots indicate the interpreted location of the of the basin structure.

ANSI

Similarly as with the Malargüe array, ANSI is also applied to a full year (2012) of data from the SPREE-array. However, as opposed to the Malargüe array, band pass filtering and whitening does provide satisfactory results for the SPREE array. Therefore, these filters are applied before autocorrelation. Figure 7-10 shows the results of this study, where Figure 7-10(a) shows the result with only a 4th-order Butterworth filter (1-3 Hz) filter and Figure 7-10(b) shows the result with the same filter as well as spectral whitening applied. The individual ANSI stacks per month are shown in Appendix B. There are no big differences between the individual months, although some seasonal variety is seen (e.g. stronger amplitudes below SN57 from May to September in the non-whitened results).
In the first 2 seconds TWT, the results of Figure 7-10 (both non-whitened as well as whitened) compare reasonably well with the GloPSI HF results presented before. However, at later times the resemblance decreases, with the ANSI results displaying a more horizontal structure as opposed to the dips still present in the GloPSI HF results. The non-whitened ANSI data display the feature at 0.5 s TWT below station SN49, which was also found by the P- and PKIKP-autocorreations (Figure 7-7). The whitened ANSI data especially show resemblance

with the combined results below stations SN47 to SN52 (Figure 7-9). A faint hint of the basin structure can also be seen in the figures, but it is not as well defined as in Figure 7-9.
The data availability of the SPREE array was quite good during this year, only station SN45 was inactive for September and October. The other stations had an average downtime of 5 days.

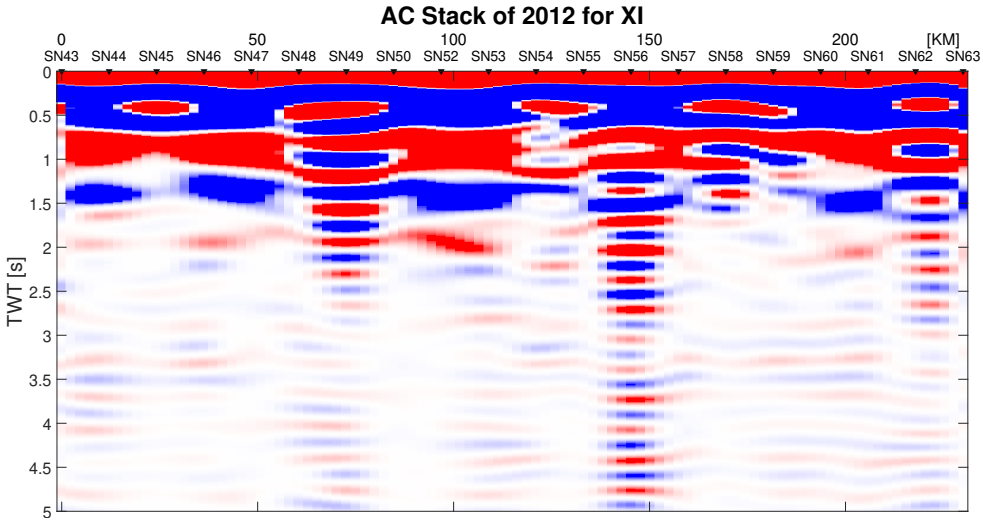

(a) No whitening applied

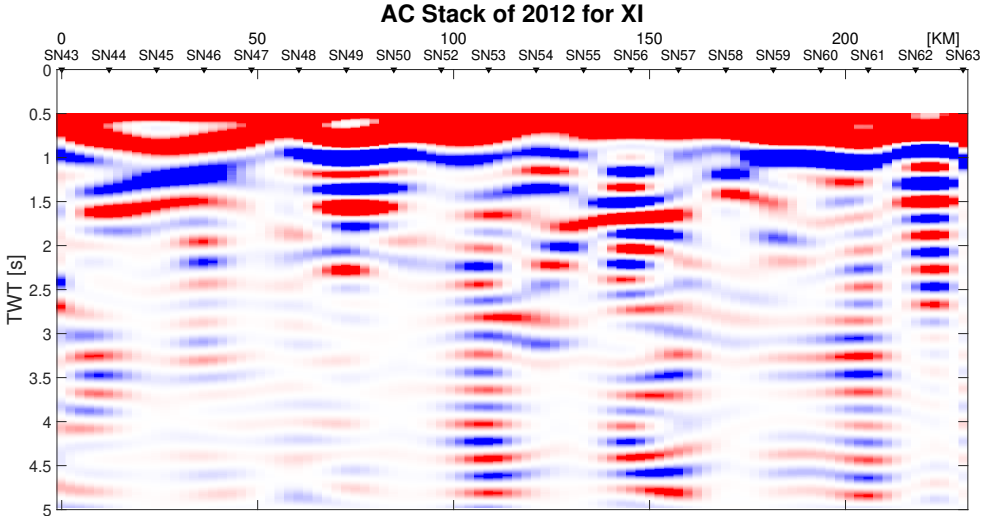

(b) Whitening applied

Figure 7-10: Full year of ANSI result for the SN-line, using a 4th-order Butterworth filter between 1 and 3 Hz. Whitening has only been applied to the bottom image.

Chapter 8

Single station high frequency analysis
USArray: H17A & 214A

Although both the Malargüe and SPREE arrays show promising results, they did not achieve the high frequencies of 8 Hz first presented by Verdel et al. (2016). Also, in the original analysis of the USArray such high frequency signal was observed (as stated in Section 4-2). In Table 8-1 the number of events possessing sufficient energy at very high frequencies ($\geq$ 6 Hz), for each of the stations is indicated. The events have a distance of at least 80 degrees to ensure that the angle of incidence of the P-events is relatively low. Moreover, because the high frequency signal is considered, the 9.9 $f_{\max}$ events are included, and, at a later stage, erroneous measurements will be excluded. Based on the table, two stations were selected for further analysis:

1. Station 214A, Organ Pipe Cactus National Monument, AZ
2. Station H17A, Yellowstone National Park, WY

The exact location of the stations can also be found in Figure 3-2. Finally, aside from the P- and PKIKP-autocorrelations on both stations, 1-year of data is autocorrelated and stacked (ANSI) to compare both methods.

Table 8-1: Table displaying the number of high frequency ($\geq$ 6 Hz) events for each selected station of the USArray (Figure 3-2), both for P- and PKIKP-events, recorded from May 2007 to April 2008.

Station	121A	214A	435B	833A	ABTX	BGNE	H17A	K22A	KSCO
P	93	151	23	37	50	36	86	56	50
PKIKP	29	43	11	22	40	15	31	19	15
Station	MSTX	N23A	O20A	Q24A	S22A	SPMN	SUSD	T25A	W18A
P	39	62	95	55	94	45	29	102	77
PKIKP	19	15	24	12	15	40	8	29	7
Station	MDND	WHTX	Y22D						
P	56	52	73						
PKIKP	19	24	34						

8-1 Geological setting

The selection of station 214A from Table 8-1 is rather obvious, since it has the highest number of events available compared to all the other stations. However, station H17A does not boast such statistics and other stations might arguably be a better choice. The reason that the station was selected anyway, is due to its location in the Yellowstone national park, which is a relatively well-studied area due to the presence of the Yellowstone Caldera. This means that the velocities below the station are quite well known, particularly the presence of a low-velocity zone (LVZ) beneath the caldera is of interest. This LVZ is likely due to crystallizing magma body (Husen et al., 2004). The compressional wave velocity, in this case, drops from 5.7 km/s to 2.3 km/s (Chu et al., 2010). This causes a strong contrast that is likely to be noticeable on a seismogram. Lü et al. (2013) located the 2-km thick LVZ layer at a depth of around 8 km, this would mean that around 2.8 s TWT[1] a reflection should be visible, and around 4.5 s TWT[2] a second reflection with reverse polarity should appear.
The geology near the 214A station is known to a lesser extent than station H17A, thus there are no expectations on the reflectors for this stations. However, by comparing the different autocorrelations (P, PKIKP, and ANSI) the accuracy of results can still be validated.

8-2 Phase correlations

Once again the phase autocorrelations are created according to Figure 6-3, with the only difference being the bandpass filter. No whitening is applied to the data and a 4th-order Butterworth filter with a low-cut of 3 Hz and a high-cut of 8 Hz is used. Furthermore, for the P-phase correlations events below magnitude 7.0 are excluded, while for PKIKP the events below magnitude 6.5 are excluded. This is done due to the fact that the low magnitude events often proofed to be erroneous rather than having a high frequency, and even with this limit sufficient events can be stacked. Finally, the number of stacks are not limited to a fixed amount, but rather all events with a suitable $f_{\max}$ are used since there will be no inconsistencies between different stations because only a single station will be evaluated (instead of making a section from multiple stations). The results of station H17A will be discussed first, followed by the results of station 214A.

Station H17A

Figure 8-1 shows the autocorrelation of the individual P-phase events in black and the final stack for the station in red. After manually removing a few ACs that were dominated by low frequency signal the final number of traces was 10. In Appendix C an overview of all the events used in this section is presented. Figure 8-2 shows the final PKIKP results; 13 events in total were used for this image. Although there is quite a lot of variations between the individual events, the two final stacks of P and PKIKP are quite similar, especially the first 0.75 seconds show close resemblance. In the final section of this chapter a more detailed comparison, also including the ANSI results, will be made.

[1] 8 km * 2 / 5.7 km/s using the formula: TWT = depth * 2 / velocity
[2] 2.8 s + (2 km * 2 / 2.3 km/s) again using TWT = depth * 2 / velocity

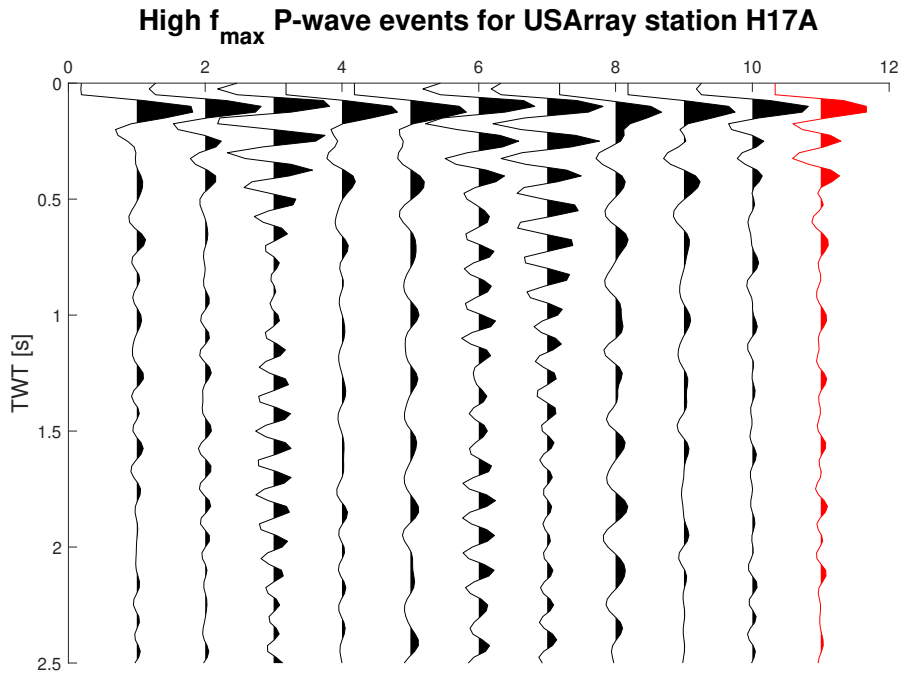

Figure 8-1: PKIKP-phase autocorrelations for station H17A of the USArray. In black the individual events are displayed, in red the full stack is shown. A 4th-order Butterworth filter between 3 and 8 Hz was applied to the data.

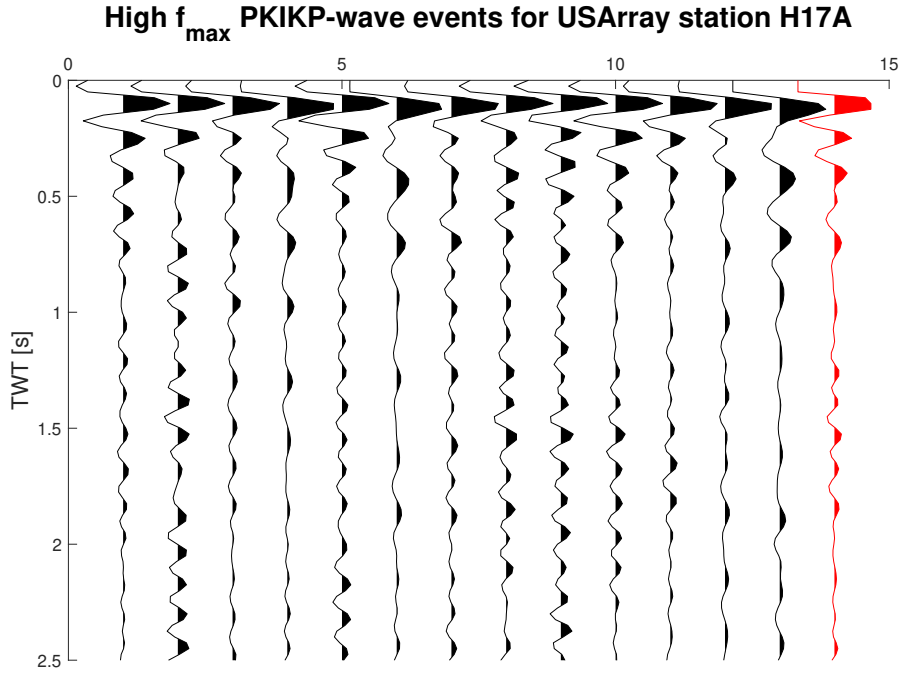

Figure 8-2: PKIKP-phase autocorrelations for station H17A of the USArray. In black the individual events are displayed, in red the full stack is shown. A 4th-order Butterworth filter between 3 and 8 Hz was applied to the data.

Station 214A

The phases for station 214A were processed in the same manner as H17A: in total 14 P-phases were used and 12 PKIKP-phases. Again, some low frequency traces were excluded, with the final results displayed in Figure 8-3 and Figure 8-4. Once more, a lot of variation can be seen between the individual traces, while the final stacks show similarities. Moreover, the signature of the first 0.5 seconds is completely different from this same time window for the H17A station, which strengthens the belief that the autocorrelation is showing receiver-side effects (and not undesired source-side structures).

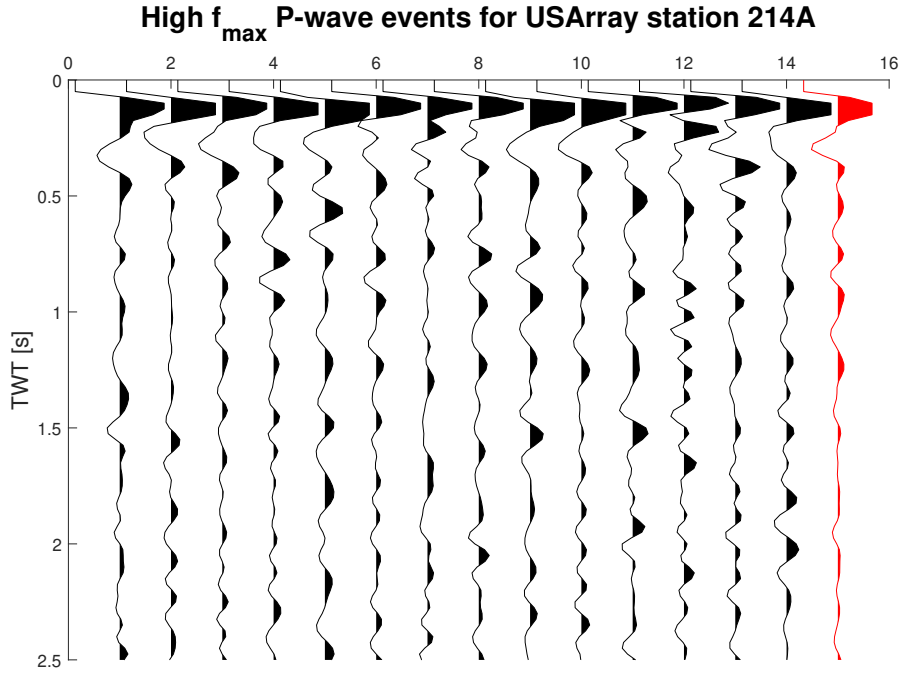

Figure 8-3: P-phase autocorrelations for station 214A of the USArray. In black the individual events are displayed, in red the full stack is shown. A 4th-order Butterworth filter between 3 and 8 Hz was applied to the data.

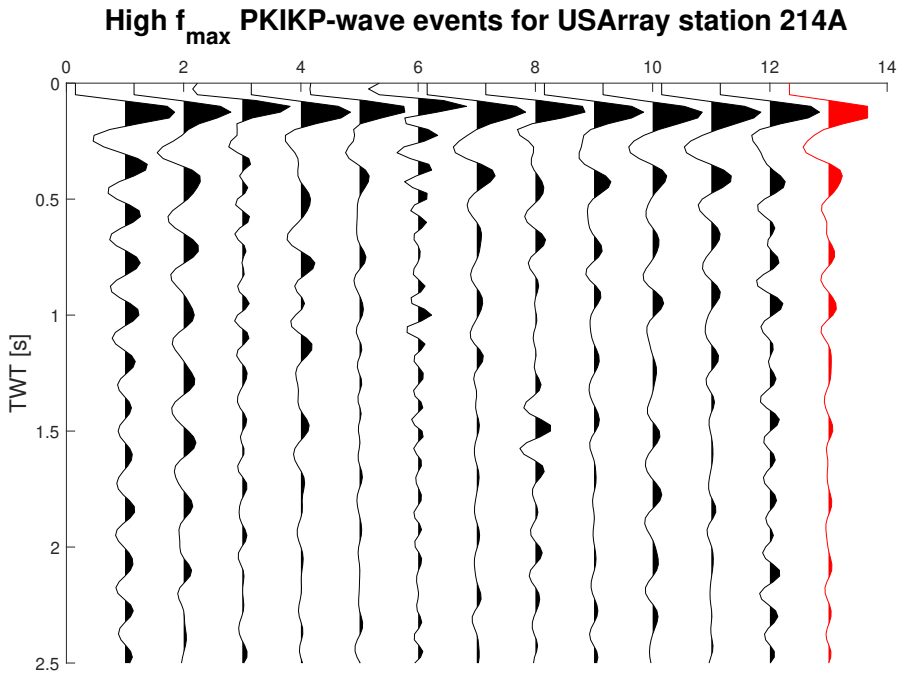

Figure 8-4: PKIKP-phase autocorrelations for station 214A of the USArray. In black the individual events are displayed, in red the full stack is shown. A 4th-order Butterworth filter between 3 and 8 Hz was applied to the data.

8-3 Ambient Noise Seismic Interferometry

For comparison with the phase-correlations, ANSI is also performed on the data. For this a full year of data is first retrieved, 2013 in this case. The data was loaded in 2-hour segments, of which 10 minutes are autocorrelated and stacked, an overlap of 50% (5 minutes) is used to limit the influence of edge effects. First, the data are deconvolved with the instrument response. Before autocorrelation a 4th-order Butterworth filter is applied to data, with the same frequencies (3-8 Hz) as the phase-correlations. After this, the data is autocorrelated and normalized, before finally stacking all the data. For each month an AC stack is saved, as well as the final stack for the full year.

Station H17A

Figure 8-5 shows the ANSI results for station H17A. The black traces are a 1-month stack and the red trace is the final year-stack. The clear seasonal variation is especially striking in the figure. In the summer (May to September) the signal seems to be more high frequency. Moreover, the traces can almost exactly be mirrored halfway through the year in July. Another noticeable feature is the peak at about 0.3 s TWT, this peak is clearly visible in the summer, while it almost completely disappears in the winter season. Finally, it would be interesting to figure out what the cause of the seasonal variation can be. A major source of noise is the oceans, which has a seasonal variation due to the occurrence of hurricanes mostly in summer.

However, the results for station 214A, which will be discussed in the next section, contradict this explanation as there is almost no seasonal variety here, while the station is located in closer vicinity to the ocean. A second possible explanation has to do with the climate in Yellowstone national park: in the months of May to October the average temperature rises above zero, while the rest of the year it drops below zero (NOAA, 2010). The variation in the seismogram almost exactly matches this variation in climate, it is, therefore, likely that these variations are somehow related. While finding the exact cause of the variations is beyond the scope of this research, some possible explanations could be the: the freezing of the Yellowstone Lake in winter and subsequent melting in summer, the melting of the glaciers in the nearby Grand Teton National Park or the increasing activity of the rivers during the summer when the ice is melting.

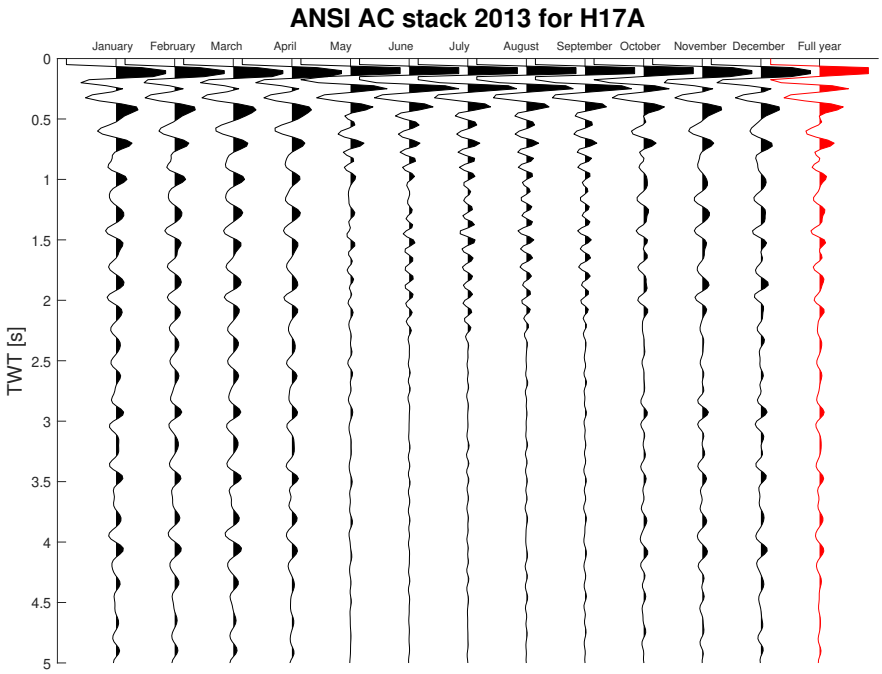

Figure 8-5: Result for ANSI at station H17A using a 4th order Butterworth filter between 3 and 8 Hz. The stacks for the individual months are shown (black) as well as the stack for the full year (red). Seasonal influence is clearly visible.

Station 214A

Lastly, the results of ANSI for station 214A are shown in Figure 8-6. As stated before, there is not nearly as much seasonal variation present in this stack. The only noteworthy changes are in amplitude and not in frequencies. Namely, the feature between 0.7 and 1 s TWT seems to be a little stronger in the winter compared to the summer. Now that all the result have been presented in this section; the next section will compare the different results of all methods.

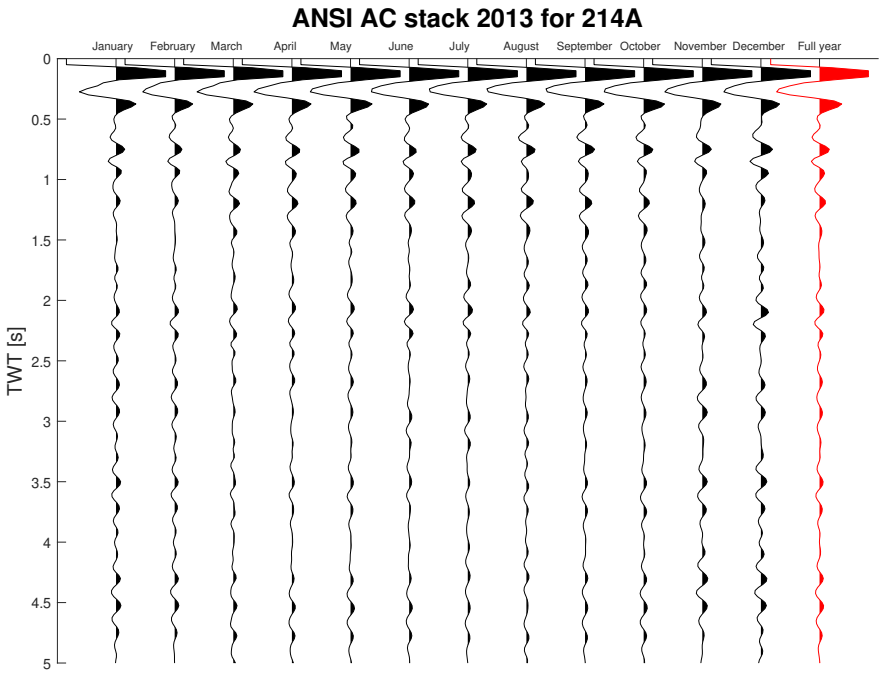

Figure 8-6: Result for ANSI at station 214A using a 4th order Butterworth filter between 3 and 8 Hz. The stacks for the individual months are shown (black) as well as the stack for the full year (red). Seasonal influence is hardly visible.

8-4 Comparison of the results

Finally, the three different methods will be compared in this section. Once again station H17A will be discussed first, followed by station 214A.

Station H17A

Figure 8-7 shows the results of the ANSI, P-phase and PKIKP-phase autocorrelations. All the traces have been plotted three times to assist the reader to better recognize structural matches (and miss-matches) between the different methods. The similarity between the three results in the first second TWT is quite obvious in the figure, as the traces look almost identical here. Figure 8-8 highlights the data from 0.5 to 7.5 s TWT; the ANSI result includes a point-source spreading-correction, as discussed in the theory section of this report (Section 2-2). This correction is done according to the divergence formulas proposed by Newman (1973) using the velocity model by Lü et al. (2013). Although the similarities might not be as strong as in the first second there are still plenty of noteworthy features to be found. For example, the negative loop at around 2.5 s TWT (marked with an A) seems to be appearing in all three results. This reflection is possibly the start of the LVZ discussed earlier in the geology (Section 8-1). This means that the reflection appears slightly earlier than the expected 2.8 seconds, suggesting that the LVZ can be found at a lower depth than expected. To support the statement that this reflection is indeed the start of the LVZ, a second reflection with

opposite polarity should be found about 1.7 seconds after the first event, associated with the deeper boundary of the LVZ. This would mean the reflection at around 4.1 s TWT (marked with a B) marks the end of the LVZ. However, this event only really stands out in the PKIKP correlations, whereas the ANSI and P results show multiple other peaks and troughs before the expected end of the LVZ. Although, this evidence may not be very compelling, the results do show that the autocorrelations did retrieve a meaningful reflection response, demonstrated by the similarities between the different methods (and the entirely different results of the 214A station).
From these results, it can be concluded that the first 3 seconds are rather similar, and the first 5 seconds are still somewhat consistent, but after this, the variation between the results of the different methods seems to be increasing rapidly. Furthermore, it should be noted that the PKIKP results are probably more accurate than the P results since the PKIKP-phases arrive at a very steep angle (around 5 degrees) compared to the P-phases (with angles between 13 and 15 degrees). This means that the P-phases are more likely to include information coming in laterally from the stations as opposed to only including information from right below the station (i.e. zero-offset information).

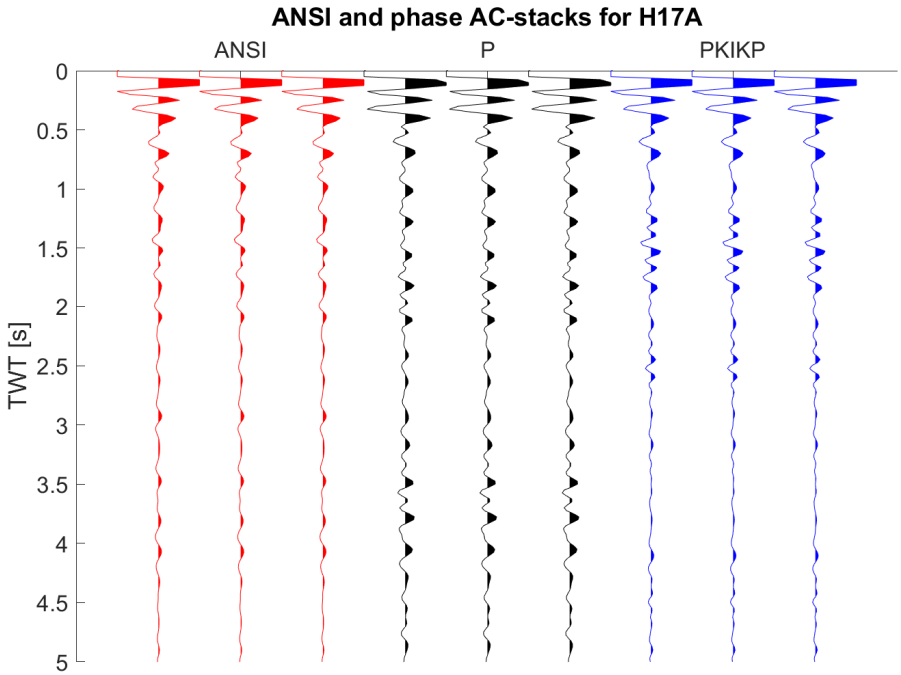

Figure 8-7: Result for ANSI (red, left), P-phase correlations (black, middle), PKIKP-phase correlations (blue, right). All traces have been plotted 3 times for easier comparison and the same 4th order Butterworth filter between 3 and 8 Hz has been applied to the data.

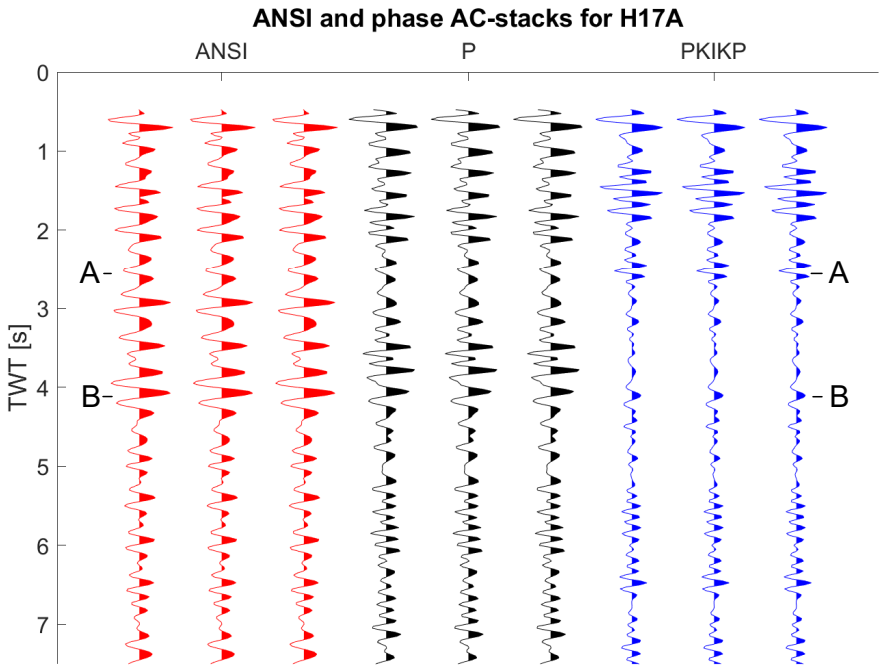

Figure 8-8: Result for ANSI (red, left), P-phase correlations (black, middle), PKIKP-phase correlations (blue, right). All traces have been plotted 3 times for easier comparison and the same 4th order Butterworth filter between 3 and 8 Hz has been applied to the data. Geometrical spreading-correction has been applied to the ANSI result, enhancing the reflections at greater depths. "A" marks the interpreted start of the LVZ, while "B" marks the end.

Station 214A

Finally, the results of station 214A will be discussed. In Figure 8-9 the resulted obtained with the different methods are plotted alongside each other. Like station H17A, for station 214A the ANSI and PKIKP correlations compare very well in the first 0.5 s TWT, but the P correlations are slightly different this time. The lower part after 0.5 s TWT is displayed in Figure 8-10. Because no velocity model was available the ANSI results are not spreading-corrected this time. Instead the maximum depth in TWT is only 5 seconds (not 7.5 seconds as before), since the spreading-correction affects larger depths more than shallow depths. Again there are a few noticeable features in the results. First of all the ANSI and PKIKP results seems to be comparing well, whereas the P results are less similar. A number of events catch the eye, for example, the troughs at 0.9 and 2.2 seconds, which are appearing in all three ACs. Secondly, the peak at 1.2 s TWT is rather prominent in all results. Below 3 seconds the resemblance between the traces seem to be decreasing. Therefore, from these results as well as the results from station H17A it can be concluded that the methods are comparing well for the first few seconds of TWT (3 s for 214A, 5 s for H17A), after which the traces start to deviate more from each other. However, in the first part, high frequency structural information can definitely be retrieved.

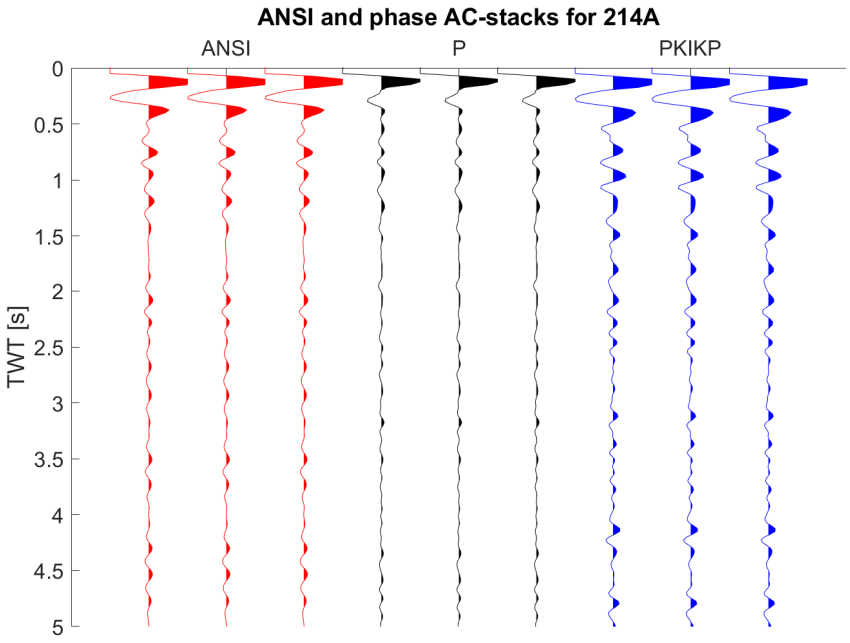

Figure 8-9: Result for ANSI (red, left), P-phase correlations (black, middle), PKIKP-phase correlations (blue, right). All traces have been plotted 3 times for easier comparison and the same 4th order Butterworth filter between 3 and 8 Hz has been applied to the data.

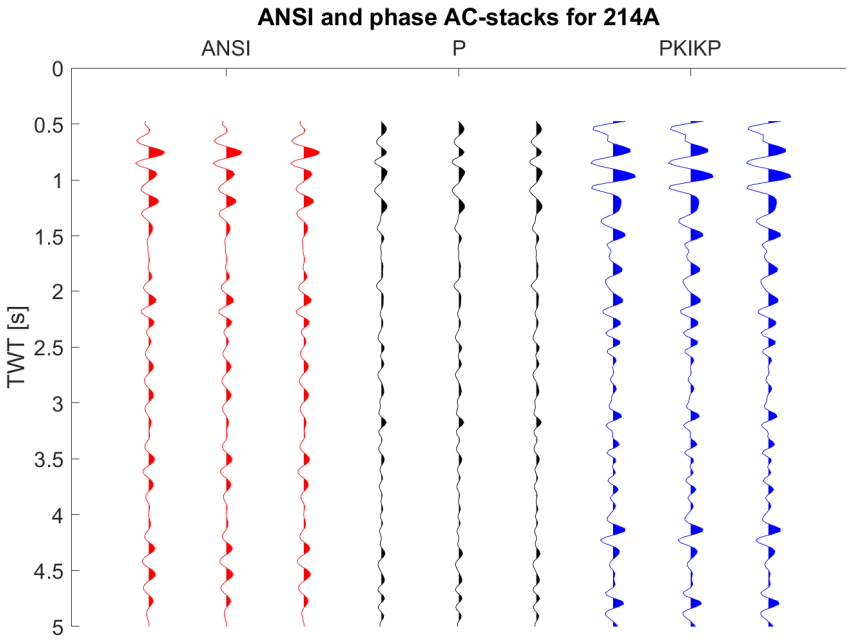

Figure 8-10: Result for ANSI (red, left), P-phase correlations (black, middle), PKIKP-phase correlations (blue, right). All traces have been plotted 3 times for easier comparison and the same 4th order Butterworth filter between 3 and 8 Hz has been applied to the data.

Chapter 9

Conclusion and discussion

Verdel et al. (2016) first noticed the potential of high frequency signal in the coda of distant earthquakes. In this research, this potential is first quantified by collecting and analyzing over a decade of earthquake data collected by 21 permanent broadband stations in the US. The large amount of data provides valuable insights into the behavior of the maximum amplitude vs distance and magnitude. We find that for increasing magnitude the maximum amplitude increases as well, while for increasing distances the maximum amplitude decreases. Furthermore, it is concluded that the PKIKP- and P-phases are most promising for GloPSI HF. The average maximum amplitude, of about 3 Hz, is sufficiently promising to perform a number of case studies.
The first case study is done on the Malargüe array, where the geology is already relatively well known. By auto-correlation of the coda of several PKIKP events we find the bottom boundary of the sedimentary basin at a few kilometers depth; these observations were in line with results from previous studies in the same area.
Below the SPREE array in the US, the second area studied, the geology is less well known. However, the array is located more optimally to also include P-phase arrivals. By combining P- and PKIKP-events in this area the method proves it's usefulness once more, by successfully imaging the basement of a suspected sedimentary basin.
The first two case studies were conducted in the 1 to 3 Hz band because the data did not allow for higher frequencies. The third case study did provide higher frequencies (3-8 Hz) on two single stations of the USArray. To compare the results of GloPSI HF with ANSI (Ambient Noise Seismic Interferometry) a noise study was also performed. The results appeared to be comparable for the first few seconds; for later two-way-times there was more deviation between the different methods. Moreover, the results show structural information beneath the stations.

While the method does succeed in imaging sedimentary boundaries, it is also found that the maximum frequency was significantly lower for this kind of subsurface. This means that the very high frequencies (larger than 3 Hz) are only achieved on stations underlain by more solid rock, which limits the areas that the method can be used in.

Secondly, for most of the images, PKIKP events are used. However, other phases (PKP and PKiKP) often arrive at approximately the same time as the PKIKP events. This means that there can be some interference of the other phases in the results. Fortunately, all these phases have a low ray parameter, ensuring a small angle of incidence, which is a requirement for successful application of the autocorrelation method.
Finally, there are some advantages and disadvantages to the proposed methods. The most important advantages include that it is a computationally cheap and fast method and that it is a passive, low effort, method. On the other hand, the success of the method is largely linked to the location of the array, as $f_{\max}$ varies quite a lot depending on the subsurface below the station. Another disadvantage is that the data needs to be recorded over longer periods of time, without knowing exactly when a suitable earthquake will occur.
It should also be noted that the P-phases should not be used for large depths ($\geq$ 3 s TWT) because there is an illumination gap for small angles of incidence (at small depths the single station analysis shows that the P-phases still provide satisfactory results). However, the relatively large angles of the P-phases do compliment the small angles of the PKIKP-phases quite well, allowing to enrich the GloPSI HF result, as shown for the SPREE-array.
The ANSI studies provides some very promising results as well. Even though the method is used in a rather crude way for the Malargüe and SPREE array, some indications about the structure below the arrays are retrieved. Of course, more research is needed to improve those results further and especially the Malargüe array could benefit from a more thorough selection of the noise to eliminate the spiky effects. Furthermore, it would be interesting to analyze the spectral content of the noise in detail, in order to gain more insights on what filters should be applied to the data. For the single stations of the USArray, the difference in seasonal effects is a very interesting phenomenon, that still is an appealing topic for further research as well. Nevertheless, the results found by the ANSI provide an exciting peek at the possibilities of the method.

Lastly, it can be said that GloPSI HF succeeded in increasing the resolution as desired, where traditionally frequencies between 0.1 and 1 Hz are used, this method allows a shift to a maximum frequency of at least 3 Hz, which can be especially useful in imaging the upper crust. In conjuction with existing geophysical prospecting methods, this method can assist in the exploration of deep ($\sim$ 5 km) geothermal or hydrocarbon reservoirs. Where it can be used to delineate the bottom of the sedimentary basins, which is an important constrain, e.g. for geothermal prospecting.

References

Boullenger, B., Verdel, A., Paap, B., Thorbecke, J., and Draganov, D. (2014). Studying CO2 storage with ambient-noise seismic interferometry: A combined numerical feasibility study and field-data example for Ketzin, Germany. *Geophysics*, 80(1):Q1–Q13. doi: 10.1190/geo2014–0181.1.

Chu, R., Helmberger, D. V., Sun, D., Jackson, J. M., and Zhu, L. (2010). Mushy magma beneath Yellowstone. *Geophysical Research Letters*, 37(1). doi: 10.1029/2009GL041656.

Claerbout, J. F. (1968). Synthesis of a layered medium from its acoustic transmission response. *Geophysics*, 33(2):264. doi: 10.1190/1.1439927.

Crotwell, H. P., Owens, T. J., and Ritsema, J. (1999). The TauP Toolkit: Flexible seismic travel-time and ray-path utilities. *Seismological Research Letters*, 70:154–160. doi: 10.1785/gssrl.70.2.154.

Dost, B., Edwards, B., and Bommer, J. J. (2018). The Relationship between M and ML: A Review and Application to Induced Seismicity in the Groningen Gas Field, The Netherlands. *Seismological Research Letters*, 89(3):1062–1074. doi: 10.1785/02201700247.

Draganov, D., Campman, X., Thorbecke, J., Verdel, A., and Wapenaar, K. (2009). Reflection images from ambient seismic noise. *Geophysics*, 74(5):A63–A67. doi: 10.1190/1.3193529.

Draganov, D. and Ruigrok, E. (2014). Passive seismic interferometry for subsurface imaging. *Encyclopedia of Earthquake Engineering*, pages 1–13. doi: 10.1007/978–3–642–36197–5_378–1 .

Draganov, D., Wapenaar, K., Mulder, W., Singer, J., and Verdel, A. (2007). Retrieval of reflections from seismic background-noise measurements. *Geophysical Research Letters*, 34(4). doi: 10.1029/2006GL028735.

Farías, M., Comte, D., Charrier, R., Martinod, J., David, C., Tassara, A., Tapia, F., and Fock, A. (2010). Crustal-scale structural architecture in central Chile based on seismicity and surface geology: Implications for Andean mountain building. *Tectonics*, 29(3). doi: 10.1029/2009TC002480.

Green, A. G., Cannon, W., Milkereit, B., Hutchinson, D., Davidson, A., Behrendt, J., Spencer, C., Lee, M., Morel-á LáHuissier, P., and Agena, W. (1989). A Glimpce of the Deep Crust Beneath the Great Lakes. *Properties and Processes of Earth's Lower Crust*, 51:65–80. doi: 10.1029/GM051p0065.

Husen, S., Smith, R. B., and Waite, G. P. (2004). Evidence for gas and magmatic sources beneath the Yellowstone volcanic field from seismic tomographic imaging. *Journal of Volcanology and Geothermal Research*, 131(3-4):397–410. doi: 10.1016/S0377–0273(03)00416–5.

Kennett, B. and Engdahl, E. (1991). Traveltimes for global earthquake location and phase identification. *Geophysical Journal International*, 105(2):429–465. doi: 10.1111/j.1365–246X.1991.tb06724.x.

Kraemer, P., Silvestro, J., Achilli, F., and Brinkworth, W. (2011). Kinematics of a hybrid thick-thin-skinned fold and thrust belt recorded in Neogene syntectonic wedge-top basins, Southern Central Andes between 35 and 36s, Malargue, Argentina. doi: 10.1306/13251340M943099.

Lü, Y., Ni, S., Xie, J., Xia, Y., Zeng, X., and Liu, B. (2013). Crustal S-wave velocity structure of the Yellowstone region using a seismic ambient noise method. *Earthquake Science*, 26(5):283–291. doi: 10.1007/s11589–013–0016–1.

Madariaga, R. (1976). Dynamics of an expanding circular fault. *Bulletin of the Seismological Society of America*, 66(3):639–666.

Moré, J. J. and Sorensen, D. C. (1983). Computing a trust region step. *SIAM Journal on Scientific and Statistical Computing*, 4(3):553–572. doi: 10.1137/0904038.

Newman, P. (1973). Divergence effects in a layered earth. *Geophysics*, 38(3):481–488. doi: 10.1190/1.1440353.

Nishitsuji, Y., Ruigrok, E., Gomez, M., and Draganov, D. (2014). GlobalPhase H/V Spectral Ratio for Delineating the Basin in the Malarge Region, Argentina. *Seismological Research Letters*, 85(5):1004. doi: 10.1785/0220140054.

Nishitsuji, Y., Ruigrok, E., Gomez, M., Wapenaar, K., and Draganov, D. (2016). Reflection imaging of aseismic zones of the Nazca slab by global-phase seismic interferometry. *Interpretation*, 4(3):SJ1–SJ16. doi: 10.1190/INT–2015–0225.1.

NOAA, U. (2010). National Climatic Data Center. *Climate of 2005*.

OpenStreetMap contributors (2004). Planet dump retrieved from https://planet.osm.org . `https://www.openstreetmap.org`.

Oren, C. and Nowack, R. L. (2016). Seismic body-wave interferometry using noise autocorrelations for crustal structure. *Geophysical Journal International*, page ggw394. doi: 10.1093/gji/ggw394.

Pawlowicz, R. (2000). M_Map: A mapping package for Matlab. *University of British Columbia Earth and Ocean Sciences.* Accessed 16-07-2018: `https://www.eoas.ubc.ca/~rich/map.html`.

Romero, P. and Schimmel, M. (2018). Mapping the Basement of the Ebro Basin in Spain With Seismic Ambient Noise Autocorrelations. *Journal of Geophysical Research: Solid Earth*, 123(6):5052–5067. doi: 10.1029/2018JB015498.

Ruigrok, E., Campman, X., Draganov, D., and Wapenaar, K. (2010). High-resolution lithospheric imaging with seismic interferometry. *Geophysical Journal International*, 183(1):339–357. doi: 10.1111/j.1365–246X.2010.04724.x.

Ruigrok, E., Draganov, D., Gomez, M., Ruzzante, J., Torres, D., Pumarega, I. L., Barbero, N., Ramires, A., Ganan, A. C., van Wijk, K., and Wapenaar, K. (2012). Malargüe seismic array: Design and deployment of the temporary array. *The European Physical Journal Plus*, 127(10):126. doi: 10.1140/epjp/i2012–12126–7.

Ruigrok, E. and Wapenaar, K. (2012). Global-phase seismic interferometry unveils P-wave reflectivity below the Himalayas and Tibet. *Geophysical Research Letters*, 39(11). doi: 10.1029/2012GL051672.

Shearer, P. M. (2009). *Introduction to seismology*. Cambridge University Press.

Shen, W., Wiens, D. A., Aleqabi, G., Wysession, M., van der Lee, S., Zhang, H., Stein, S., Frederiksen, A., Darbyshire, F., Wolin, E., and Bollmann, T. (2016). A clearer look at a giant scar that underlies the American Midwest. `https://www.earth.northwestern.edu/spree/nuggets/SPREE_crust2.htm`. Accessed: 2018-08-07.

Snieder, R. (2004). Extracting the Greens function from the correlation of coda waves: A derivation based on stationary phase. *Physical Review E*, 69(4):046610. doi: 10.1103/PhysRevE.69.046610.

Stamen Design (2011). Stamen Terrain Map Style. `https://stamen.com`.

Stein, S., Stein, C. A., Klee, J., Keller, R., Merino, M., Wolin, E., Weins, D., Wysession, M. E., Al-Equabi, G., Shen, W., Frederiksen, A., Darbyshire, F., Jurdy, D., Waite, G., Rose, W. I., Vye, E., Rooney, T., Moucha, R., and Brown, E. (2016). New Insights into North Americas Midcontinent Rift. *EOS*, 97(18):10–16. doi: 10.1029/2016EO056659.

Stein, S., Van Der Lee, S., Jurdy, D., et al. (2011). Learning from failure: The SPREE mid-continent rift experiment. *GSA Today*, 21(9):5–7. doi: 10.1130/G120A.1.

Storchak, D. A., Schweitzer, J., and Bormann, P. (2003). The iaspei standard seismic phase list. *Seismological Research Letters*, 74(6):761. doi: 10.1785/gssrl.74.6.761.

Tibuleac, I. M. and von Seggern, D. (2012). Crustmantle boundary reflectors in Nevada from ambient seismic noise autocorrelations. *Geophysical Journal International*, 189(1):493–500. doi: 10.1111/j.1365–246X.2011.05336.x.

Van Der Lee, S., Revenaugh, J., Wiens, D., and Wysession, M. (2013). Superior Province Rifting Earthscope Experiment (SPREE). `http://www.usarray.org/researchers/obs/flexible/deployments/1116_SPREE/`. Accessed: 2018-05-18.

Verdel, A., Wedemeijer, H., Paap, B., Vandeweijer, V., Weemstra, C., Jousset, P., Franke, S., Blanck, H., Águstsson, K., and Hersir, G. P. (2016). Reykjanes ambient noise reflection

interferometry. *Proceedings European Geothermal Congress 2016, Strasboug, France, 19-24 Sept 2016, ISBN: 978–2–9601946–0–9*.

Wapenaar, K., Draganov, D., Snieder, R., Campman, X., and Verdel, A. (2010). Tutorial on seismic interferometry: Part 1 - Basic principles and applications Tutorial on interferometry: Part 1. *Geophysics*, 75(5):75A195–75A209. doi: 10.1190/1.3457445.

Weemstra, C., Draganov, D., Ruigrok, E. N., Hunziker, J., Gomez, M., and Wapenaar, K. (2017). Application of seismic interferometry by multidimensional deconvolution to ambient seismic noise recorded in Malargüe, Argentina. *Geophysical Journal International*, 208:693–714. doi: 10.1093/gji/ggw425.

Appendix A

$f_{\max}$ histograms

In Chapter 4 it is stated that the fitting function produced outliers at $f_{\max}$ equal to 9.9 Hz. This is shown in this appendix, firstly Figure A-1 shows the histograms for three magnitude bins: 6.4-6.6, 7.8-8.0 and 8.8-9.0. Secondly, Figure A-2 shows the histograms for three distance bins: 30-40, 80-90 and 140-150 degree. The figures show the data with and without outliers.

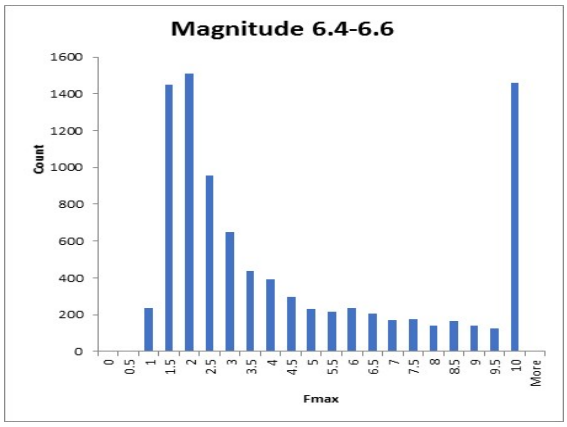

(a) Magnitude 6.4-6.6 including outliers

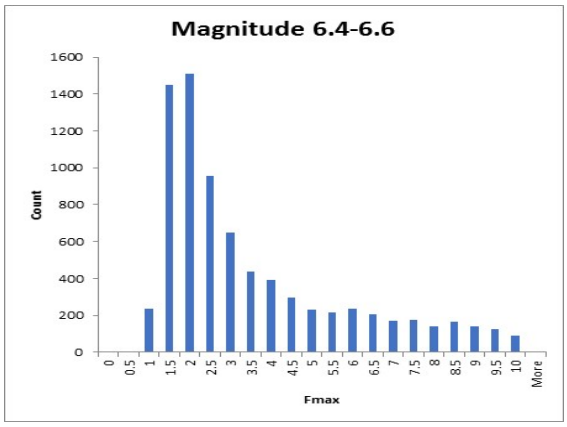

(b) Magnitude 6.4-6.6 excluding outliers

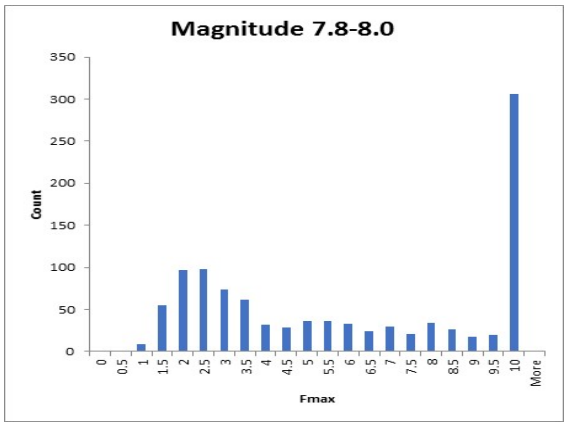

(c) Magnitude 7.8-8.0 including outliers

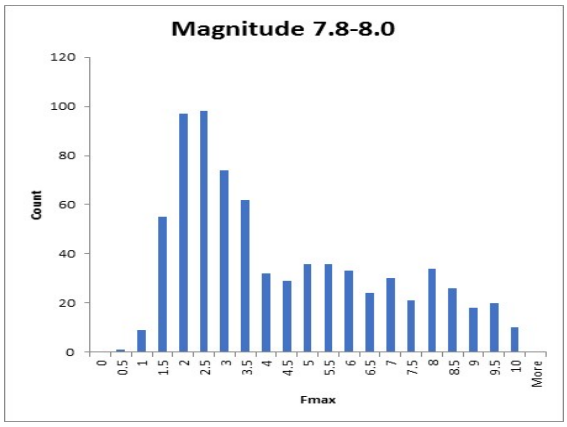

(d) Magnitude 7.8-8.0 excluding outliers

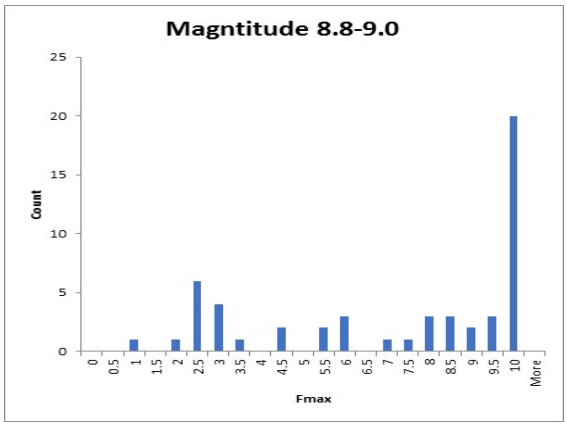

(e) Magnitude 8.8-9.0 including outliers

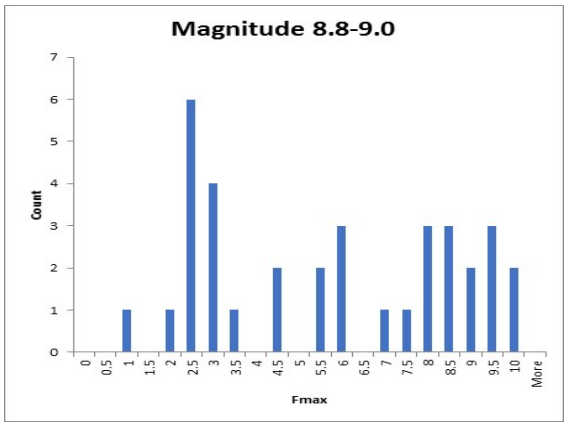

(f) Magnitude 8.8-9.0 excluding outliers

Figure A-1: Histograms showing the distribution of f_{max} for different magnitudes. The outliers are included on the left and removed on the right figures.

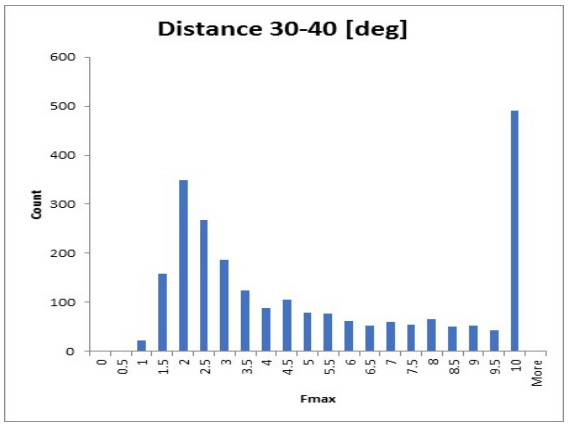

(a) 30-40 deg including outliers

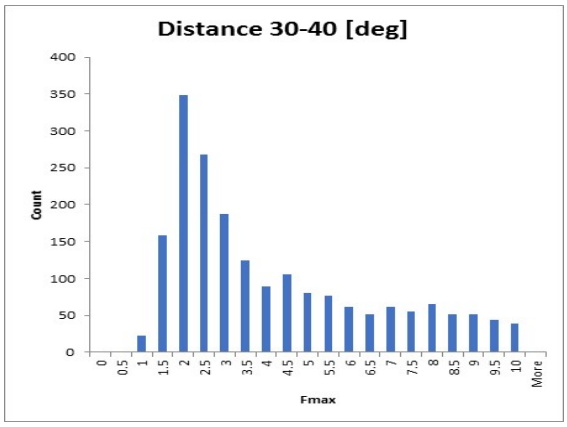

(b) 30-40 deg excluding outliers

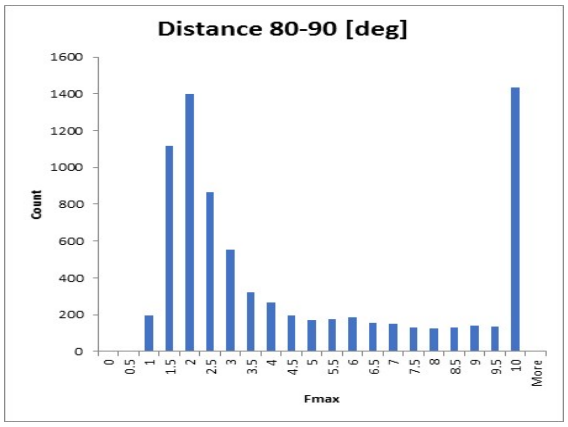

(c) 80-90 deg including outliers

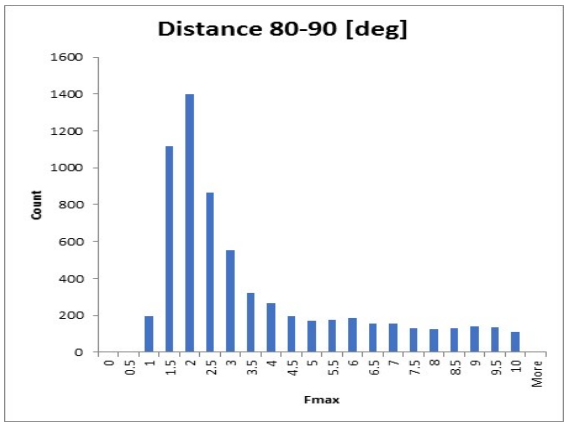

(d) 80-90 deg excluding outliers

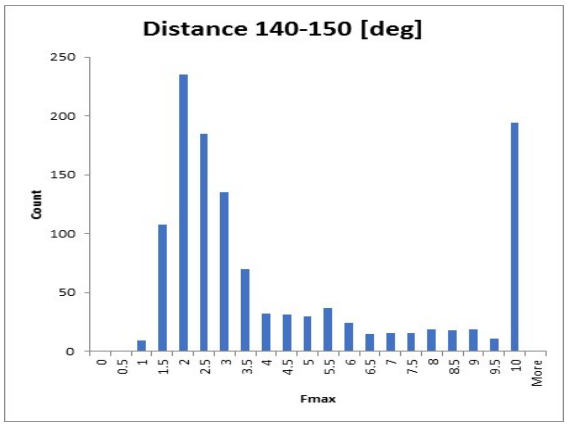

(e) 140-150 deg including outliers

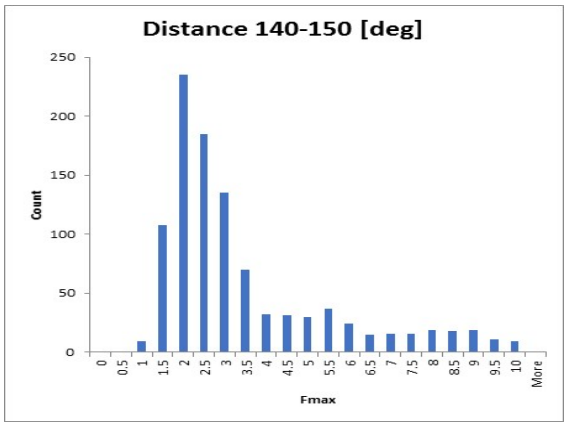

(f) 140-150 deg excluding outliers

Figure A-2: Histograms showing the distribution of f_{max} for different distances. The outliers are included on the left and removed on the right figures.

Appendix B

Monthly ANSI gathers SPREE array

Chapter 7 shows the full 2012 autocorrelation stacks for ANSI. In this appendix the monthly results for the ANSI studies are presented as well. In Figure B-1 the results for the ANSI without whitening are shown and in Figure B-2 the whitened results are displayed.

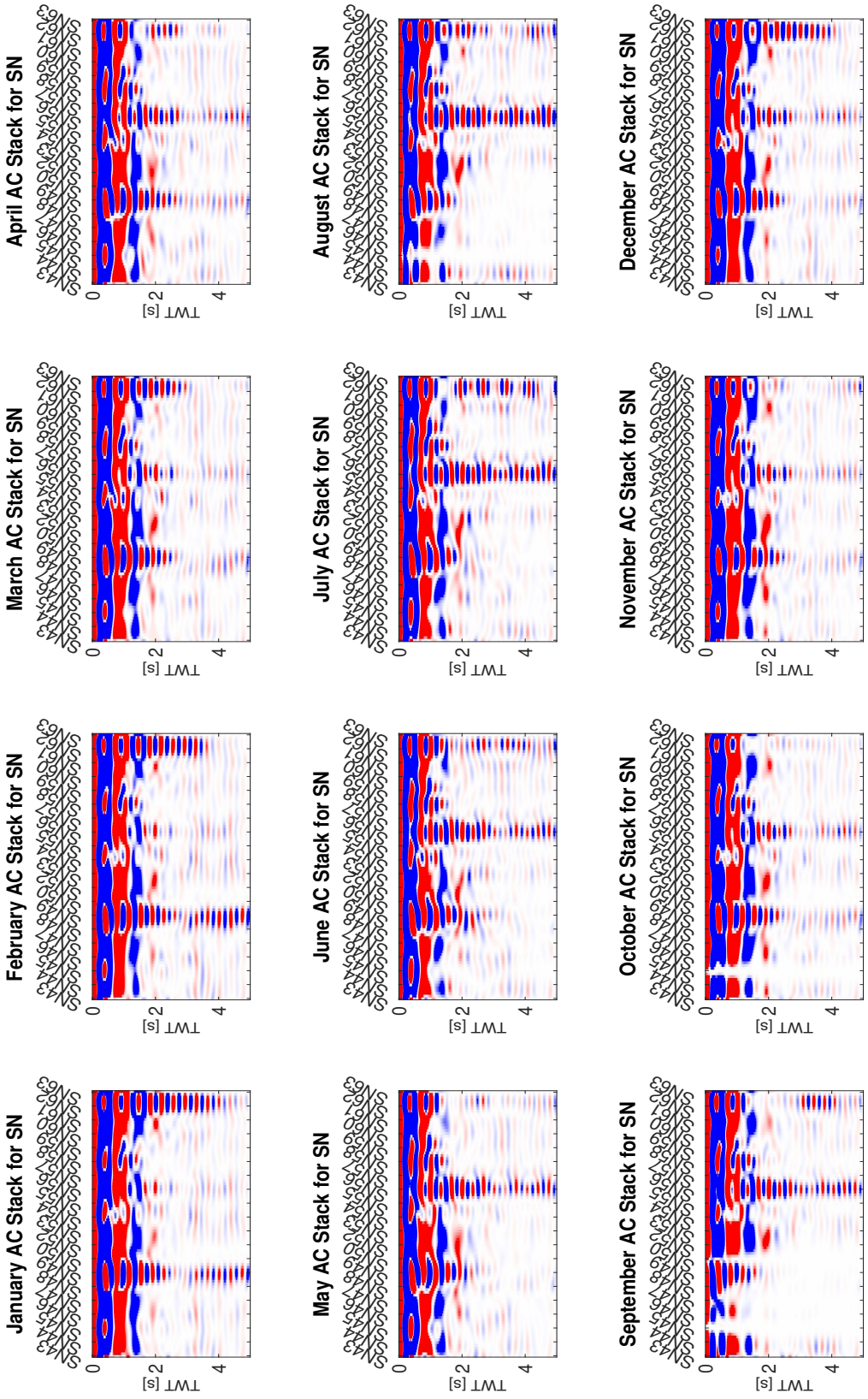

Figure B-1: ANSI results per month of the SN-line, a 4-th order Butterworth filter between 1 and 3 Hz has been applied to the data.

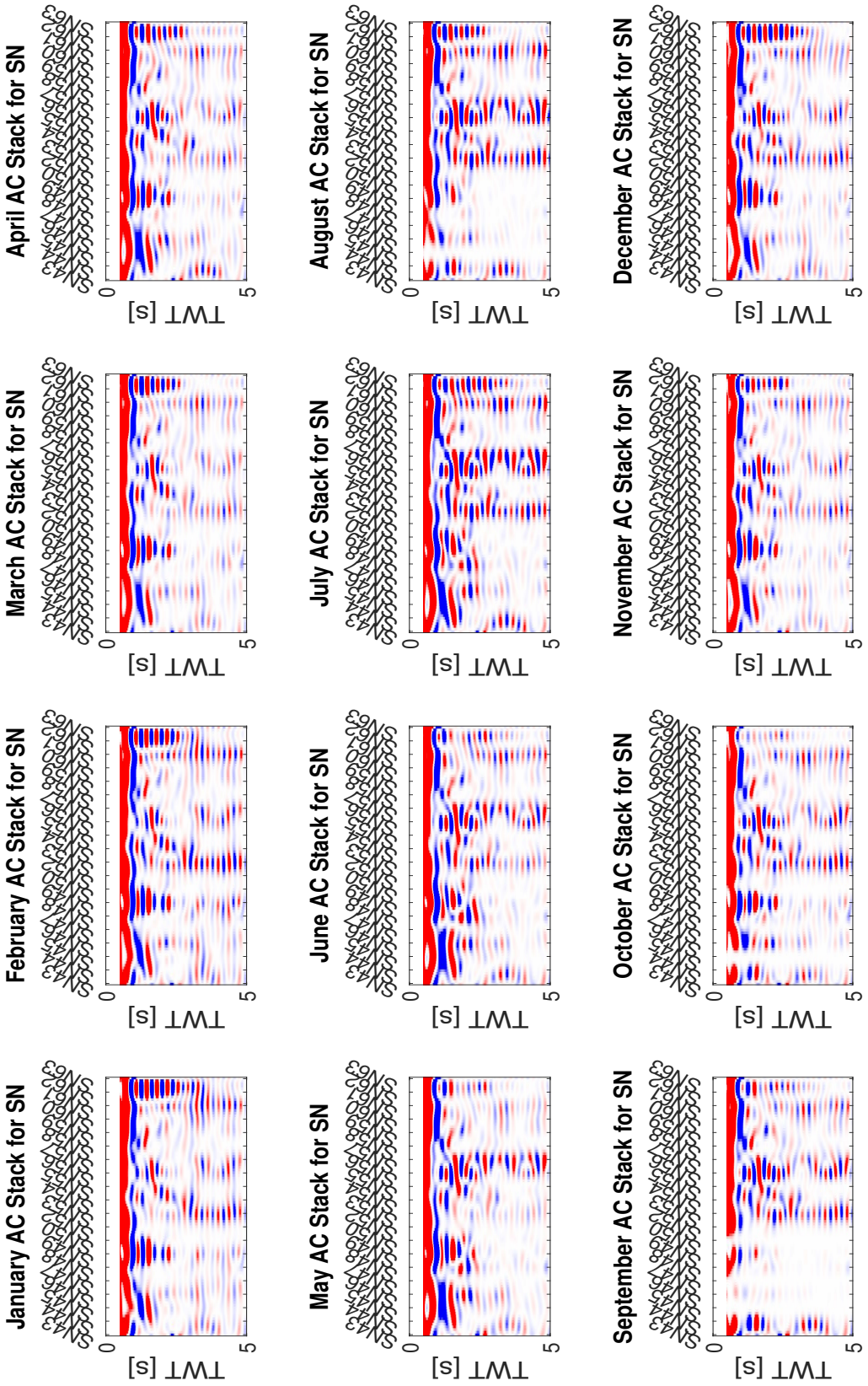

Figure B-2: ANSI results per month of the SN-line, spectral whitening and a 4-th order Butterworth filter between 1 and 3 Hz has been applied to the data.

Appendix C

Event tables

For the USArray stations in Chapter 8, a number of P- and PKIKP-events are used. In this appendix, the details of these events are listed. This includes the date and time of the earthquake, the depth, magnitude and origin (using the back azimuth and distance), the ray parameter and the calculated fields of the corner frequency, maximum frequency and angle of incidence. First the P-events are listed for station H17A in Table C-1 and station 214A in Table C-2. Secondly the PKIKP-events can be found in Table C-3 (H17A) and Table C-4 (214A).

P

Table C-1: P-events used for station H17A

Station	Date	Time	Depth [km]	Mag	Back Azi	Dist [deg]	f_c [Hz]	f_{max} [Hz]	p [s/km]	AoI [deg]
H17A	12-25-16	14:22:27	38	7.6	159.49	93.68	0.014	9.781	0.041	13.56
H17A	04-15-16	16:25:06	10	7	262.84	84.8	0.035	8.523	0.045	14.86
H17A	10-20-15	21:52:02	135	7.1	231.78	94.86	7.973	9.998	0.041	13.45
H17A	2-06-13	01:54:15	9.9	7	234.24	92.83	0.025	9.998	0.041	13.62
H17A	2-06-13	01:23:23	34	7.1	234.18	93.98	0.008	9.998	0.041	13.54
H17A	10-21-11	17:57:17	34.8	7.4	219.35	94.47	0.016	8.373	0.041	13.5
H17A	12-21-10	17:19:41	13.8	7.4	258.4	81.73	0.031	9.998	0.047	15.55
H17A	3-11-10	14:55:29	24.4	7	155.78	86.21	0.019	9.29	0.044	14.52
H17A	02-27-10	08:01:23	35	7.4	158.67	88.22	0.019	9.848	0.043	14.05
H17A	1-03-10	22:36:29	29.8	7.1	237.52	97.63	0.018	6.765	0.04	13.22

Table C-2: P-events used for station 214A

Station	Date	Time	Depth [km]	Mag	Back Azi	Dist [deg]	f_c [Hz]	f_{max} [Hz]	p [s/km]	AoI [deg]
214A	09-01-16	16:37:57	19	7	222.57	93.96	0.033	9.998	0.041	13.55
214A	08-29-16	04:29:57	10	7.1	109.59	94.25	0.039	9.456	0.041	13.53
214A	04-15-16	16:25:06	10	7	270.49	91.77	0.033	9.998	0.042	13.68
214A	07-18-15	02:27:33	11	7	241.68	88.86	0.052	9.998	0.042	13.91
214A	05-07-15	07:10:19	10	7.1	246.13	96.04	0.037	9.998	0.041	13.38
214A	03-29-15	23:48:31	41.3	7.5	247.84	96.43	0.017	9.998	0.04	13.33
214A	04-12-14	20:14:38	15.3	7.6	242.07	91.81	0.017	9.998	0.042	13.68
214A	02-08-13	15:26:38	22.4	7	241.11	88.3	0.045	9.965	0.043	14.04
214A	03-09-11	02:45:19	26.2	7.3	274.36	80.45	0.029	9.998	0.048	15.82
214A	05-27-10	17:14:46	34.7	7.2	239.43	89.39	0.021	8.323	0.042	13.77
214A	02-26-10	20:31:26	24.2	7	266.71	97.71	0.035	8.923	0.04	13.21
214A	03-19-09	18:17:40	30.9	7.6	227.02	80.75	0.015	9.573	0.048	15.75
214A	09-29-08	15:19:30	35	7	224.77	87.31	0.031	9.498	0.043	14.26
214A	09-02-07	01:05:19	37.5	7.2	240.83	88.94	0.018	9.998	0.042	13.87

PKIKP

Table C-3: PKIKP events used for station H17A

Station	Date	Time	Depth [km]	Mag	Back Azi	Dist [deg]	f_c [Hz]	f_{max} [Hz]	p [s/km]	AoI [deg]
H17A	05-29-17	14:35:21	12	6.6	248.45	117.72	0.069	9.998	0.017	5.71
H17A	10-19-16	00:26:01	614	6.6	248.9	127.93	0.071	9.998	0.017	5.64
H17A	11-04-15	03:44:15	20	6.5	245.02	120.16	6.924	9.998	0.017	5.7
H17A	04-15-14	03:57:01	10	6.8	133.55	140.4	0.042	9.998	0.016	5.34
H17A	9-01-13	11:52:32	135.2	6.5	244.73	117.28	0.06	9.998	0.017	5.71
H17A	10-09-12	12:32:08	12.1	6.6	217.07	130.04	7.515	9.998	0.017	5.62
H17A	07-26-12	05:33:33	16.2	6.6	110.88	153.03	0.074	9.998	0.013	4.34
H17A	04-16-09	14:57:06	17.6	6.7	146.39	124.6	0.034	9.998	0.017	5.68
H17A	06-27-08	11:40:15	27.6	6.6	256.24	121	0.051	9.998	0.017	5.7
H17A	6-01-08	14:31:01	10	6.5	218.64	131.48	6.753	9.998	0.017	5.6
H17A	02-25-08	18:06:05	33.1	6.6	250.82	130.13	0.072	9.998	0.017	5.62
H17A	11-10-07	01:13:38	22.7	6.6	218.66	122	8.398	9.998	0.017	5.69
H17A	4-11-12	08:38:37	26.3	8.6	253.14	128.83	0.019	9.998	0.017	5.64

Table C-4: PKIKP-events for station 214A

Station	Date	Time	Depth [km]	Mag	Back Azi	Dist [deg]	f_c [Hz]	f_{max} [Hz]	p [s/km]	AoI [deg]
214A	05-12-15	07:05:19	15	7.3	268.3	117.59	0.022	9.998	0.017	5.71
214A	09-24-13	11:29:48	15.5	7.8	91.86	121.11	0.022	9.998	0.017	5.7
214A	07-15-13	14:03:41	19.9	7.3	141.81	116.48	0.025	9.998	0.017	5.71
214A	04-16-13	10:44:19	63.1	7.7	91.51	119.88	0.028	9.998	0.017	5.7
214A	12-10-12	16:53:09	161.5	7.1	251.06	116.54	0.035	9.998	0.017	5.71
214A	07-23-10	22:51:13	584.7	7.7	257.54	114.05	0.023	9.998	0.017	5.71
214A	06-12-10	19:26:50	31.4	7.5	260.54	133.7	0.031	9.998	0.017	5.55
214A	04-06-10	22:15:02	33.4	7.8	258.19	135.47	0.026	9.998	0.017	5.51
214A	11-16-08	17:02:32	28.1	7.3	255.47	118.32	0.024	9.998	0.017	5.71
214A	02-25-08	08:36:33	29.8	7.2	256.17	137.4	0.03	9.998	0.016	5.45
214A	09-12-07	23:49:04	36	7.9	256.05	136.94	0.02	9.998	0.016	5.47
214A	04-11-12	08:38:37	26.3	8.6	258.45	137.94	0.018	9.998	0.016	5.43